10418–10435 *Nucleic Acids Research, 2022, Vol. 50, No. 18* *Published online 15 September 2022*
https://doi.org/10.1093/nar/gkac786

Negative supercoils regulate meiotic crossover patterns in budding yeast

Taicong Tan[1], Yingjin Tan[1], Ying Wang[1], Xiao Yang[1,2,3,4,5], Binyuan Zhai[1,2,3,4,5], Shuxian Zhang[1,6], Xuan Yang[1], Hui Nie[7], Jinmin Gao[7], Jun Zhou[7], Liangran Zhang[1,6,7,*] and Shunxin Wang[1,2,3,4,5,*]

[1]Center for Reproductive Medicine, Cheeloo College of Medicine, State Key Laboratory of Microbial Technology, Shandong University, China, [2]National Research Center for Assisted Reproductive Technology and Reproductive Genetics, Shandong University, Jinan, Shandong 250012, China, [3]Key Laboratory of Reproductive Endocrinology of Ministry of Education, Jinan, Shandong 250001, China, [4]Shandong Provincial Clinical Research Center for Reproductive Health, Jinan, Shandong 250012, China, [5]Shandong Key Laboratory of Reproductive Medicine, Jinan, Shandong 250012, China, [6]Advanced Medical Research Institute, Shandong University, Jinan, Shandong 250012, China and [7]Center for Cell Structure and Function, Shandong Provincial Key Laboratory of Animal Resistance Biology, College of Life Sciences, Shandong Normal University, Jinan 250014, Shandong, China

Received April 24, 2022; Revised August 21, 2022; Editorial Decision August 23, 2022; Accepted September 01, 2022

ABSTRACT

Interference exists ubiquitously in many biological processes. Crossover interference patterns meiotic crossovers, which are required for faithful chromosome segregation and evolutionary adaption. However, what the interference signal is and how it is generated and regulated is unknown. We show that yeast *top2* alleles which cannot bind or cleave DNA accumulate a higher level of negative supercoils and show weaker interference. However, *top2* alleles which cannot religate the cleaved DNA or release the religated DNA accumulate less negative supercoils and show stronger interference. Moreover, the level of negative supercoils is negatively correlated with crossover interference strength. Furthermore, negative supercoils preferentially enrich at crossover-associated Zip3 regions before the formation of meiotic DNA double-strand breaks, and regions with more negative supercoils tend to have more Zip3. Additionally, the strength of crossover interference and homeostasis change coordinately in mutants. These findings suggest that the accumulation and relief of negative supercoils pattern meiotic crossovers.

INTRODUCTION

Meiosis produces haploid gametes from diploid progenitor cells. The formation of crossover recombination (CO), a reciprocal exchange of flanking markers between homologous chromosomes (homologs), is a hallmark of meiosis. Meiotic COs ensure faithful chromosome segregation and promote genetic diversity by shuffling alleles between homologs.

Different organisms share a common meiotic recombination process, which is integrated into the meiotic chromosome where a linear array of loops is anchored on a proteinaceous axis at their bases(1–5). Meiotic recombination initiates from the conserved Spo11 complex mediated programmed DNA double-strand breaks (DSBs) (6–10). DSBs are resected to generate 3' single-stranded DNA (ssDNA) overhangs. One ssDNA end invades a homolog template to form a displacement loop (D-loop) and promotes DNA synthesis (2,3). If this invading strand is released from the template and anneals with the other ssDNA end, the DSB will be repaired as a noncrossover (NCO) via the synthesis-dependent strand annealing (SDSA) pathway (11,12). However, if the nascent D-loop is stabilized, a recombination intermediate, single-end invasion, will be formed and then the second DSB end will be captured to form a double Holliday junction (dHJ), which is most likely to be resolved as a CO (12–14).

It has been widely accepted that there are two types of COs (2–3,15–17). In most organisms, the formation of a majority (70–90%, depending on the organism) of COs (Class I) requires a group of conserved ZMM proteins, which includes at least Zip1-4, Msh4/5, Mer3 and Spo16 in budding yeast (2–3,3,18). Zip3 (its orthologues RNF212 and HEI10 in other organisms) and MLH1/3 are enriched on this type of CO sites as bright foci on pachytene chromosomes (15,19–23). The rest, a minority of COs (Class II) requires Mms4 and Mus81, which is thought to arise from a different pathway (2,3,15–17).

*To whom correspondence should be addressed. Tel: +86 531 88364286; Email: zhangliangran@sdu.edu.cn
Correspondence may also be addressed to Shunxin Wang. Tel: +86 531 88364286; Email: shunxinwang@sdu.edu.cn

Both the number and distribution of crossovers are tightly regulated. As a result, each pair of homologs obtains at least one CO (the obligatory CO) and multiple COs tend to be evenly spaced on a chromosome. The latter phenomenon is known as CO interference, which was discovered a century ago (1–3,16,24,25). Numerous studies suggest that only Class I COs are interference-dependent and thus patterned by CO interference, however, Class II COs are interference insensitive [reviewed in (2,3,15–17)].

CO interference spreads along chromosomes with microns of axis length as a metric to inhibit the further occurrence of COs nearby, and thus proper CO interference requires intact chromosome axes (1,15). The interplay between CO interference and axis length largely determines CO frequency and distribution, which has an important role in evolutionary adaption (5,25–27). Besides the obligatory CO and CO interference, the meiotic CO pattern shows a third conserved feature, CO homeostasis, which describes the phenomenon that alterations in meiotic DSBs result in no or less proportional alterations in CO numbers (1,4,15,28,29). It is usually considered that these three phenomena are regulated in a single process, among which CO homeostasis results from CO interference, and the strength of CO homeostasis depends on the strength of CO interference (1,15,21,28,30). However, what the interference signal is and how it is generated and regulated is largely unknown.

Previously, we identified a pathway regulating CO interference, among which Topoisomerase II (Top2) plays a central role. This finding supports the stress-relief model (15,21). Mechanical stress, arising from chromosome axis-constrained global chromatin expansion, accumulates along chromosome axes and provokes local crossover designation which intrinsically results in local stress relief (i.e. generating interference). The local change redistributes outwards along chromosome axes (spreading of interference) and results in chromatin/axis compaction and thereby suppresses additional crossover designations. Top2 may act during the compaction process to adjust spatial relationships among DNA segments within the axes and thus implement both local relief of stress (interference) and its redistribution (21). However, how Top2 regulates this process is unknown.

In this study, we elucidated the mechanism of Top2 regulating crossover interference. Top2 regulates DNA supercoils and catenation by an ATP-dependent strand-passage reaction (31–33), which probably affects chromatin stress (34). We examined CO patterns in strains expressing different *top2* alleles, which affect different steps of the strand-passage reaction, and in strains expressing different *Escherichia coli* topoisomerases, which regulate either DNA supercoils or catenation or both. Our results showed that yeast strains, either *top2* alleles or ectopically expressing bacterium topoisomerases, accumulating more (less) negative supercoils have weaker (stronger) CO interference and more (less) COs. Moreover, yeast Top2 affects CO interference and thus CO frequency in a dosage-dependent fashion. Further investigations showed that negative supercoils accumulated preferentially at CO-associated Zip3 regions before CO designation and regions with more negative supercoils tend to have higher Zip3 enrichment. These findings suggest that the CO patterning process involves the accumulation and relief of negative supercoils, which is the possible mechanical stress regulating CO designation and interference.

MATERIALS AND METHODS

Yeast strains

All *Saccharomyces cerevisiae* strains used in this study were derived from the SK1 background and were listed in Supplementary Table S1. Plasmids were listed in Supplementary Table S2.

Yeast strains with *top2* alleles were constructed by inserting a linearized plasmid with *top2* alleles into the *URA3* locus. The plasmids containing *top2* alleles are a kind gift from Prof. D.J. Clark (32). The 3HA tagged *TOP2* and *top2* alleles strains were constructed by inserting a triple-HA tag to the C-terminus by the PCR method. The P_{CUP1}-TOP2 strain was constructed by the one-step PCR method to replace the native promoter with the inducible *CUP1* promoter (35). The yeast strains expressing *Escherichia coli* topoisomerases (with yeast *TOP2* promoter) were constructed by one-step PCR to integrate the plasmids into yeast. The plasmids were constructed by inserting the yeast *TOP2* promotor and *Escherichia coli* topoisomerase ORF into the backbone of the pRS42N plasmid (36). Double and triple mutants were constructed by the standard genetic cross and tetrad dissection. All strains were confirmed by PCR and DNA sequencing.

Yeast meiotic synchronization and time-course analysis

Yeast meiotic cultures were synchronized with the SPS pregrowth method as previously described (37). Yeast cells were grown in SPS II medium (0.5% yeast extract, 1% peptone, 0.67% yeast nitrogen base without amino acids, 1% potassium acetate, 0.05 M potassium biphthalate, pH5.5) for 16–18h to a density of 10^8 cells/ml. Yeast cells were collected and resuspended in an equal volume of sporulation medium SPM (2% potassium acetate, 0.02% raffinose) to induce yeasts to initiate meiosis. To induce P_{CUP1}-*TOP2* expression, $CuSO_4$ was added at 2 h after SPM induction. To inhibit strand passage reaction (SPR) of Top2, 1 mg/ml etoposide (Sigma-Aldrich, Cat# E1383) or 0.15 mg/ml ICRF-193 (Sigma-Aldrich, Cat# I4659) was added at 2 h in SPM. At each hour, 100μl meiotic culture was taken, and cells were fixed with 50% ethanol in 0.1 M Sorbitol and stained by 4,6-diamidino-2-phenylindole (DAPI; Sigma-Aldrich, Cat# D9542). Meiotic nuclear divisions were monitored under a microscope (AxioImager.Z2) with an EMCCD camera (Andor, iXon Ultra 888).

Sporulation efficiency and spore viability assays

Cells at 24 h in SPM were collected to analyze sporulation efficiency and spore viability. Sporulation efficiency was determined by calculating the frequency of yeast cells with asci under light microscopy. More than 200 cells were counted for each strain. For each strain, 96 tetrads were dissected onto YPD plates under a dissection microscope (Sporeplay,

Singer Instruments) and incubated at 30°C for 2 days. Spore viability was calculated as the percentage of viable spores.

Chromosome spreads and immunofluorescence

The surface spread of meiotic nuclei was performed with the Lipsol method as previously described (21). Briefly, yeast cells collected at proper time points from synchronized meiotic cultures were treated into spheroplasts with Zymolyase 100T (Ncalai Tesque, Cat# M9K5593), spread on a clean slide with 1% lipsol and immediately fixed by 3% paraformaldehyde containing 3.4% sucrose. For immunofluorescence, slides with surface spread nuclei were incubated with primary antibodies and then secondary antibodies. The following primary antibodies were used in this study: rabbit monoclonal anti-Top2 (TopoGEN, Cat# TG2014; 1:1000 dilution); mouse monoclonal anti-Myc (Santa Cruz Biotechnology, Cat# sc-40; 1:1000 dilution); goat polyclonal anti-Zip1 (Santa Cruz Biotechnology, Cat# sc-48716; 1:500 dilution); rabbit polyclonal anti-GFP (Thermo Fisher Scientific, Cat# A11122; 1:1000 dilution); rabbit polyclonal anti-Rad51(Santa Cruz Biotechnology, Cat# sc-33626; 1:1000 dilution). The following secondary antibodies were used in this study: Alexa 488-conjugated donkey anti-mouse (Thermo Fisher Scientific, Cat# A32776; 1:1000 dilution), Alexa 488-conjugated donkey anti-rabbit (Thermo Fisher Scientific, Cat# A32814; 1:1000 dilution) Alexa 555-conjugated donkey anti-rabbit (Thermo Fisher Scientific, Cat# A32794; 1:1000 dilution), Alexa 594-conjugated donkey anti-goat (Thermo Fisher Scientific, Cat# A11058; 1:1000 dilution). Chromosome DNA was stained by 4,6-diamidino-2-phenylindole (DAPI; Sigma-Aldrich, Cat# D9542). Fluorescence images were acquired using a Zeiss fluorescence microscope (AxioImager.Z2) with an EMCCD camera (Andor, iXon Ultra 888).

Mapping the positions of Zip3 foci along chromosomes

The positions of each Zip3 focus along a chromosome were determined as previously reported (21,37). Images for Zip3, Zip1 and *LacO*/LacI–GFP staining were merged and aligned using the ImageJ software (https://imagej.nih.gov/ij/). Only the GFP-marked chromosome separated from other chromosomes was analyzed. The segmented line-tracing tool of ImageJ was used to trace the positions of each Zip3 focus along the Zip1 line from the GFP marked end to the other end of the chromosome. In this way, the total length of the Zip1 line (the chromosome) was also recorded.

Quantification of immunofluorescence intensity

Top2 fluorescence intensities of WT and mutants were measured and quantified using ImageJ (https://imagej.nih.gov/ij/) as previously described (37). Briefly, wild type and mutants were mixed and spread on the same slide. Zip3 of wild type but not the mutant was 13Myc tagged, allowing the mutants and wild type to be distinguished by immunostaining Zip3-13Myc. Images from WT and mutants were photographed with the same exposure intensity and time. The fluorescence intensity was measured by ImageJ. DAPI stained chromosomal region was circled and the total (i.e. the raw intensity) and each pixel of Top2 fluorescence intensity of this area were recorded. To determine the background level, a line across the nucleus was drawn and the intensity curve for this line was displayed. The pixel intensity at approximately horizontal positions of the curve was defined as the average fluorescence intensity per pixel of the background. The Top2 intensity for the nucleus was determined as the raw intensity by subtracting the background intensity.

Western blotting

For each sample, $\sim 2 \times 10^8$ yeast cells were fixed and lysed in 20% trichloroacetic acid (TCA) using glass beads. The resultant pellet was extracted with Laemmli buffer and denatured in boiling water for 5 min, then the proteins were separated on an 8% SDS-PAGE gel and transferred to nitrocellulose filter membranes. The following antibodies were used for western blotting: mouse monoclonal anti-HA (Sigma-Aldrich, Cat# 9658; 1:5000 dilution); mouse monoclonal anti-PGK1 (Abcam, Cat# ab113687; 1:5000 dilution). Membranes were imaged with a Bio-Rad Imager. Quantification of protein bands was performed using ImageJ software.

Crossover interference analysis

Crossover interference was calculated by the classical method of coefficient of coincidence (CoC), beam-film simulation, modified coefficient of coincidence (MCoC; 21), and gamma distribution analysis (15,37). For crossover interference analysis, one end of chromosome XV or III was marked with the *LacO*/LacI-GFP. The SC length and positions of CO maker Zip3 on chromosomes XV and III were accurately measured with ImageJ software as previously described (21). In each experiment, about 200 nuclei were examined for each strain.

Coefficient of coincidence (CoC) analysis of crossover interference

For CoC analysis of crossover interference, all chromosome lengths were normalized to 100% and the position of each Zip3 focus was also correspondingly normalized. Chromosomes XV and III were divided into 30 and 10 intervals, respectively, with equal size (~0.1 μm in length) as previously described (15). Each Zip3 focus was assigned to a specific interval based on its relative position on the chromosome. For each interval, the frequency of chromosomes having at least one Zip3 focus was calculated. For each pair of intervals, the 'observed' frequency of double crossovers is defined as the frequency of chromosomes having Zip3 foci in both intervals on the same chromosome; the 'expected' frequency of double crossovers is defined as the product of the crossover frequencies for the two individual intervals. The CoC is the ratio of the 'observed' frequency of double crossovers to the 'expected' frequency of double crossovers. A CoC curve is obtained when CoC values for all possible interval pairs are plotted against their corresponding 'inter-interval distance' (the distance between the midpoints of the two inter-

vals). For simplicity, the mean of CoC values from all interval pairs with equal inter-interval distances is used to obtain a CoC curve. For a classical CoC curve, the CoC value is zero or very small at short inter-interval distances and gradually increased to ∼1 at larger inter-interval distances. This means the strength of crossover interference dissipates along with increasing distance. The inter-interval distance at which the value of CoC = 0.5, defined as L_{CoC}, can be used as a convenient measurement for interference strength although it is not so accurate. In this study, CoC curves were calculated by using a MATLAB application (https://app.box.com/s/hv91q2nrtq0cp9n8iy9m) as previously described (15). Since crossover interference spreads along the chromosome axis and is usually measured as microns of axis length, the inter-interval distance for the fraction of axis length was converted to microns.

Modified coefficient of coincidence (MCoC)

Another method of measurement of crossover interference is called modified CoC, MCoC (21). Similar to CoC analysis, chromosomes were also divided into intervals. Each interval can be used as a reference interval to divide chromosomes into two groups. One group of chromosomes has one or more crossovers (Zip3 foci) in this reference interval (CO^+_R) and the rest is divided into the other group which is the absence of crossovers in this reference interval (CO^-_R). Its nearby interval is used as a test interval (T). For each reference group (CO^+_R or CO^-_R), chromosomes are further divided into two groups based on whether there is or there is not a crossover in the test interval, i.e. CO^+_T and CO^-_T. To determine whether there is a crossover in the reference interval that interferes with the occurrence of a crossover in the test interval, Fisher's exact test is applied to decide whether the number of chromosomes bearing a crossover in the test interval in CO^+_R group is significantly lower than that in CO^-_R group. If the answer is yes, it means that the existence of a crossover in the reference interval interferes with the occurrence of a crossover in the test interval, i.e. the interference from the reference interval spreads to that test interval to reduce the probability of occurrence of another crossover. If the answer is no, it means that the existence of a crossover in the reference interval does not significantly interfere with the occurrence of a crossover in the test interval. This test can be done for all nearby intervals of a given reference interval and the result reveals the number of test intervals (and thus the distance) over which interference extends outward from the reference interval. This distance is defined as L_{MCoC}, which can be calculated for all reference intervals.

Beam-film simulation

The beam-film model is also called the 'fill-in-the-hole' model and the MATLAB application used for best-fit simulations has been described (15,34,38). The application can be downloaded at 'https://app.box.com/s/hv91q2nrtq0cp9n8iy9m'. Values of all parameters for best-fit simulations of crossovers (Zip3 foci) along WT yeast chromosomes are described (15). To get the best-fit simulation of crossover patterns in a mutant, parameters are adjusted to define the optimal values such that the average crossover number, the simulated distribution of crossover numbers per bivalent, the CoC curve, and the frequency of chromosomes absence of a crossover match the experimentally observed.

Gamma distribution analysis

Gamma distribution describes the frequency distribution of distances between adjacent COs on chromosomes and is often used to measure the interference strength. A larger (smaller) shape parameter (γ) of gamma distribution usually is interpreted as stronger (weaker) interference (15,37). The inter-adjacent Zip3 focus distances were calculated using the Zip3 focus data for CoC analysis. The best-fit gamma distribution and shape parameter (γ) for inter-adjacent Zip3 focus distances were calculated using the 'gamfit' function in MATLAB (MathWorks) via the maximum likelihood method.

Crossover homeostasis analysis

Crossover homeostasis indicates the ability to maintain crossover level when DSB is altered (28). It has been proposed that the strength of crossover homeostasis is determined by the strength of crossover interference (21,28,30). The number of crossovers can be altered by altering the number of DSBs. When the number of DSBs is altered, a series of numbers of crossovers are obtained correspondingly. If the numbers of crossovers are plotted against their corresponding DSB numbers, a curve for the strength of crossover homeostasis is obtained. A crossover homeostasis curve can be obtained experimentally using a series of strains with different numbers of DSBs. An analog theoretical crossover homeostasis curve can be obtained by simulations. Based on a given set of best-fit parameters, the average number of crossovers can be predicted by beam-film simulations. By altering the values of the precursor number *N* over the desired range, the average numbers of crossovers can be achieved corresponding to each value of *N*. The strength of crossover homeostasis can be predicted when the average numbers of crossovers are plotted against their corresponding precursor number N (15,21). In this study, the number of crossovers was evaluated by the crossover-associated Zip3 foci along chromosomes XV in a series of strains giving different levels of DSBs. DSB levels were decreased by a series of *spo11* hypomorphic alleles (*spo11-HA/spo11-HA, spo11-Y135F/spo11-HA,* and *spo11-D290A/spo11-HA*) as previously described (21,28). A *tel1* mutant was also involved in this analysis to give an increased number of DSBs. DSB levels were increased above WT levels using a *tel1*△ mutation. Such analysis was performed in a *TOP2* (with WT level of crossover interference), P_{CLB2}-*TOP2* (with decreased crossover interference), and *top2-L475A* backgrounds (with increased crossover interference). The experimental and theoretical curves can be compared when they are plotted together.

bTMP chromatin immunoprecipitation

Psoralen preferentially intercalates into negative supercoiled DNA and has been widely used to detect negative su-

percoils. Detection of negative supercoil by bTMP (biotin-4,5,8-trimethylpsoralen) was performed as previously described in yeast (39). Briefly, 10ml synchronized meiotic culture (~10^9 cells) was incubated with 0.1% sodium azide for 30 min at 30°C to block the cell cycle progression and preserve the most prevalent topological state. Yeast cells were washed with buffer A (25 mM MES, pH 6.5) and permeabilized with 0.1% digitonin (Sigma-Aldrich, Cat# D5628) for 30 min at 30°C to promote bTMP to enter cells. Permeabilized yeast cells were washed with TE buffer (10 mM Tris, 1 mM EDTA, pH8.0) and incubated with bTMP (200 μg per 10^9 cells; Thermo Fisher Scientific, Cat# 29986) in the dark for 30 min. Then yeast cells were cross-linked by 365 nm UV light to form a covalent linkage between DNA and bTMP. Cells were washed twice with ice-cold PBS and lysed in 1ml of lysis buffer (50 mM HEPES–KOH pH 7.5, 140 mM NaCl, 1 mM EDTA, 1% Triton X-100, 0.1% Na-deoxycholate) by Tissue Lyser (Qiagen Tissue Lyser II). Crosslinked chromatin was sheared to 200–500 bp by 12 × 10 s pulses using a Biorupter sonicator. Genomic DNA was purified after being treated with 100 μg/ml RNase A and 100 μg/ml proteinase K. 5% purified DNA was treated as input DNA for subsequent experiments. 5μg purified DNA was incubated with 30μl Dynabeads MyOne streptavidin (Invitrogen, Cat# 65001) overnight at 4°C. The beads were washed the following buffers sequentially: wash buffer I (20 mM Tris–HCl pH 8.0, 2 mM EDTA, 150 mM NaCl, 1% Triton X-100, 0.1% SDS), wash buffer II (20 mM Tris–HCl pH 8.0, 2 mM EDTA, 500 mM NaCl, 1% Triton X-100, 0.1% SDS), wash buffer III (250 mM LiCl, 10 mM Tris pH 8.0, 0.5% Na-deoxycholate, 0.5% NP-40, 1 mM EDTA), and TE buffer (10 mM Tris pH 8.0, 2 mM EDTA). The above washing process was repeated once. The ChIP–DNA was eluted from the beads with 250 μl elution buffer (95% formamide, 10 mM EDTA) at 90 °C for 20 min and purified with a Qiagen PCR clean-up kit (QIAGEN, Cat# 28106). To exclude topology-independent bTMP binding, bTMP binding on naked and fragmented DNA (thus no supercoils) was used as the negative control. Genomic DNA was isolated from yeast cells with the TIANamp Yeast DNA kit (TIANGEN, Cat# DP307). Isolated DNA was sheared to an average size of 200–500 bp by 6 × 10 s pulses using a biorupter sonicator (SONICS & MATERIALS, Cat# VCX130). 5 μg naked DNA was incubated with bTMP at 30°C for 30 min in the dark and cross-linked with UV at 365 nm. DNA was washed with 70% ethanol and incubated with Dynabeads MyOne streptavidin (Invitrogen, Cat# 65001) overnight at 4°C. The ChIP-DNA was washed and eluted as described above. All ChIP and input DNA were used for library preparation.

Preparation of ChIP library

Library preparation was performed using Universal DNA Library Prep Kit (Vazyme, Cat# ND607) and VAHTS DNA Adapters set1 for Illumina sequencing (Vazyme, Cat# N801). ChIP and input DNA was end-repaired and efficiently ligated to Illumina adapters with different indexes. Adapter ligation products were purified with the magic bead (Roche, Cat# 07983298001) and amplified by PCR with 12 cycles. Amplified DNA was incubated with the magic bead to select fragments between 200 and 500 bp. After selection, DNA was washed with 80% ethanol and eluted with 30 μl TE buffer. Libraries were paired-end 150 bp (PE150) sequenced using the Illumina NovaSeq platform at the company Annoroad Gene (Annoroad Gene Tech. (Beijing, China) Co., Ltd).

Processing of Illumina sequence data

The raw reads were filtered based on the quality value (q20 and q30) using FASTX Toolkit (Version 0.0.14). The filtered reads were aligned to the *Saccharomyces cerevisiae* reference genome (SacCer2, 2008) using BOWTIE2 (Version 2.4.2; (40)) to create BAM files. The BAM files were normalized to reads per kilobase per million (RPKM) by using DEEPTOOLS (Version 3.3.2; (41)). Fold enrichment for each sample was determined by comparing the signal ratio between normalized ChIP and input for every bin (bin = 50 bp) across the whole genome using DEEPTOOLS (Version 3.3.2). For peak calling, paired-end BAM was set as input file format, the effective genome size was set to 1.21×10^7 bp, and MACS2 (Version 2.1.1; (42)) was used with the following parameters: Nomodel mode, 200 bp extension size, the cutoff of FDR (q-value) at 0.05, and without broad region for peaks. The peak file was output in BED format.

Definition of negative supercoil peaks

bTMP intercalates preferentially into negative supercoil regions and is a credible maker for negative supercoil (39,43). As previously described (39,43), the bTMP enrichment was calculated as the ratio of the bTMP signal between normalized ChIP and input for each sample. To correct the negative supercoil-independent binding of bTMP, a negative control was performed and subtracted from the bTMP binding in cells. In this negative control, the naked genomic DNA was fragmented (and thus no supercoils), treated with bTMP, and then ChIP-seq was performed. This bTMP ChIP-seq result would be independent of supercoils and used as the negative control. As previously described, the ratio of bTMP binding in cells to bTMP binding in naked genomic DNA (negative control), i.e. ($bTMP_{cell}$ ChIP/input)/($bTMP_{negative\ control}$ ChIP/input), gives the normalized bTMP signal, which represents the negative supercoils-dependent bTMP enrichment (39,43). The genomic regions with normalized bTMP ratio above 1 were defined as negative supercoil peaks.

Immunostaining of bTMP-treated samples

1ml synchronized yeast meiotic cells were incubated with sodium azide to block the cell cycle and digitonin to permeabilize the cell membrane (39,44). Then, cells were incubated with bTMP and cross-linked by UV. Cells were resuspended with 100 μl buffer B (200 mM Tris pH 7.5, 20 mM EDTA pH 8.0, 1 M NaCl) and incubated with 0.6 μl β-mercaptoethanol for 10min. After being washed with buffer C (20 mM KH_2PO_4, 1.2 M sorbitol, 4.5 mM sodium citrate), cells were resuspended with 100 μl buffer D (20 mM KH_2PO_4, 20 mM K_2HPO_4, 0.5 mM MgCl, 1.2 M sorbitol) and incubated with 1 μl β-mercaptoethanol and 2 μl 5 mg/ml Zymolyase-100T for 30 min at 37°C. Treated

cells were collected by centrifugation, and resuspended with 100 μl MES buffer (1 M sorbitol, 0.1 M MES, 0.5 mM MgCl, 1 mM EDTA, pH 6.5). For nuclei spread, cells were squashed on a cleaned glass slide with a coverslip and immediately frozen at –20°C for 5min. After the coverslip was removed, slides with squashed samples were dried at room temperature. For bTMP immunofluorescence, slides were incubated with DyLight 488 labeled NeutrAvidin Protein (1:500; Thermo Fisher Scientific, Cat# 22832) for 2 h in the dark at room temperature. Chromosome DNA was stained by DAPI. Fluorescence images were acquired using a Zeiss fluorescence microscope (AxioImager.Z2). bTMP intensity was quantified using ImageJ as described above.

Quantitative reverse transcription PCR (RT-qPCR)

Total RNA was extracted from the synchronized meiotic cells at the indicated time points by using the Spin Column Yeast Total RNA Purification Kit (Sangon Biotech, Cat# B518657-0050). About 500ng of total RNA was reverse transcribed to cDNA with a HiScript™II RT SuperMix (Vazyme, Cat# R223-01). The cDNA was diluted by 3 folds and 1.5μl cDNA was used for qPCR with 2X Universal SYBR Green Fast qPCR Mix (ABclonal, Cat# RK21203) in a LightCycle 96 Real-Time PCR system (Roche). All reactions were performed in triplicate. The mRNA levels of *TOP2* in different samples were normalized to *ACT1*. Primers used for RT-qPCR were as follows: *TOP2* forward (TGG GTT CTA CTT CCG CTA C) and reverse (TTG TTT CCT GAC TGG CTT C); *ACT1* forward (AGG AAA TCA CCG CTT TGG CT) and reverse (TGT GGT GAA CGA TAG ATG GAC C).

Quantification and statistical analysis

The signal on the Western blot was quantified by ImageJ. Fluorescent images were captured under a Zeiss AxioImager.Z2 microscope with an EMCCD camera (Andor, iXon Ultra 888). Fluorescence intensity was quantified by ImageJ. Zip3 number and fluorescence intensity of Top2 and bTMP were presented as means ± SD. CoC analysis, Zip3 number distribution from experimental data and simulations, and Top2 abundance detected by western blot were presented as means ± SEM. Sample sizes (n) for each experiment are described in corresponding figure legends. The statistical significance in the mean value of events between different groups was performed by student's t-test. Two proportion Z-test was used to determine the significance levels of frequency differences between samples. The statistical significance was indicated in figures and figure legends: n.s. (not significant), $P \geq 0.05$; $^{*}P < 0.05$; $^{**}P < 0.01$; $^{***}P < 0.001$. Pearson's correlation analysis was used to calculate the correlation coefficient using EXCEL or GraphPad Prism.

RESULTS

Meiotic CO patterns in WT (wild-type) yeast

In budding yeast, patterned COs are marked by CO-correlated Zip3 foci on pachytene chromosomes (19–21,45). The position of each Zip3 focus could be accurately visualized and measured along synaptonemal complexes of surface-spread pachytene chromosomes (Figure 1A). On a given genetic chromosome, the number distribution of patterned COs was obtained by examination of Zip3 foci in more than 200 pachytene nuclei (Figure 1B and Supplementary Table S3).

CO interference suppresses the occurrence of another CO nearby, thus increasing the distance between adjacent COs and making them tend to be evenly spaced along any given chromosome (15). CO interference can be accurately and reliably described by the classical analysis of the CoC (coefficient of coincidence) curve (Figure 1C; Materials and Methods) (15,46,47). In this analysis, chromosomes are divided into multiple intervals, for a given pair of intervals, the frequency of COs in both intervals (observed double COs) is divided by the product of the frequencies of COs that occurred in each interval (expected double COs). The quotient is the CoC. A CoC curve can be made when each CoC is plotted against the corresponding inter-interval distance. As previously reported, Zip3 foci along chromosomes III and XV showed typical CoC relationships (Figure 1B, D, Supplementary Tables S3 and S4) (15,21). At a very short inter-interval distance, CoC is very small, suggesting strong interference. CoC is gradually increased along with increased inter-interval distance, suggesting gradually decreased interference. Finally, CoC fluctuates around 1, indicating no interference (independent occurrence of COs in the two intervals). The two examined chromosomes showed nearly identical CoC curves and thus the same strength of CO interference (Figure 1B, D, Supplementary Tables S3 and S4). As previously reported, the inter-interval distance corresponding to CoC = 0.5 (L_{CoC}) is a useful and convenient parameter describing the interference strength (15,21). Both chromosomes showed $L_{CoC} = 0.3$ μm (Figure 1B, D, Supplementary Tables S3 and S4).

Previously, based on the 'fill-in-the-holes' model, we developed an approach to quantitatively simulate CO patterns (a.k.a. beam-film simulation; 15,34,38). This approach accurately describes CO patterns in many organisms and successfully identified the first CO interference pathway, human female-specific CO maturation inefficiency, and co-variation of COs among chromosomes within nuclei (21,26,48). In this simulation, the parameter (L) directly reflects the CO interference, i.e. the distance over which the interference signal spreads. Using parameters previously described (15,21), simulations successfully captured CO patterns on chromosomes III and XV, including the average CO number per chromosome, the number distribution of COs among chromosomes, and especially the CoC curve and thus the strength of CO interference (Figure 1B, D, Supplementary Tables S3 and S4; Materials and Methods).

Three types of *top2* mutants with different CO patterns

Top2 plays an important role in regulating CO interference in budding yeast meiosis (21). Top2 regulates DNA supercoils and catenation by an ATP-dependent strand-passage reaction. This process requires Top2 to bind to and cleave one DNA double-strand segment (gate-segment or G-segment) to create a gate or opening, transport the

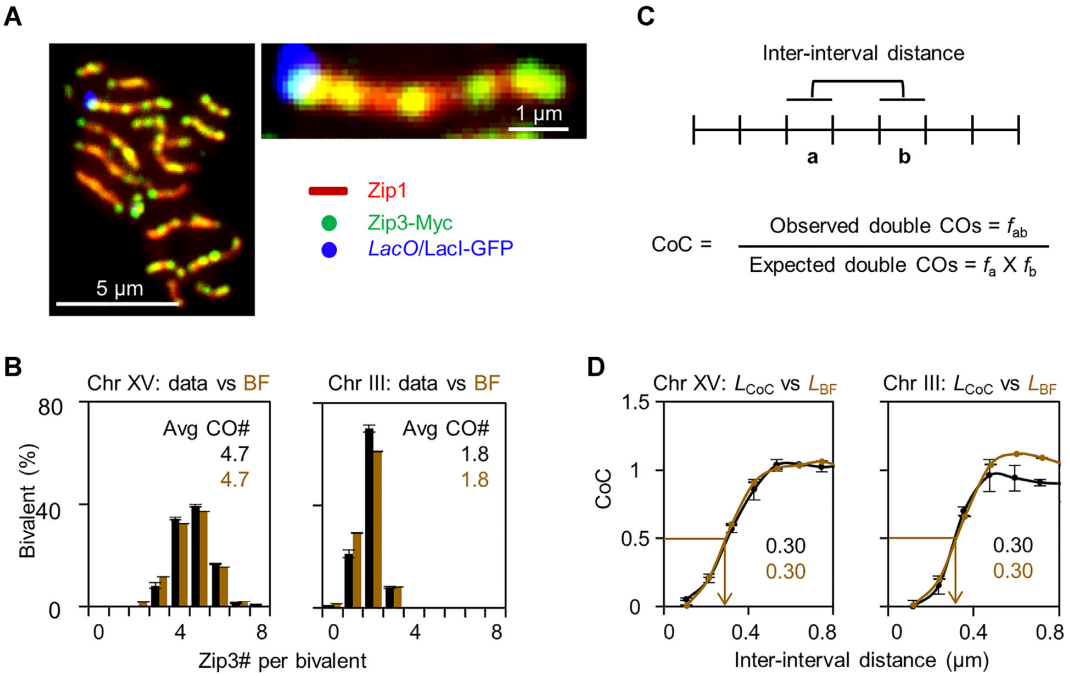

Figure 1. Meiotic CO patterns in WT yeast. (**A**) Visualization of Zip3 foci in surface-spread pachytene nuclei (5 h in SPM). Green, CO-correlated Zip3-Myc foci visualized by an anti-Myc antibody; red, synaptonemal complex Zip1 visualized by an anti-Zip1 antibody; blue, *LacO*/LacI-GFP focus on chromosome XV visualized by an anti-GFP antibody. Scale bar, 5μm (1μm in the magnified image). (**B**) Distribution of the numbers of Zip3 foci on chromosome XV (left) and III (right) in WT (black), and the best-fit simulations (dark yellow). The average number of COs was shown. (**C**) Illustration of the analysis of the coefficient of coincidence (CoC). CO, crossover. (**D**) Coefficient of coincidence on chromosomes XV and III calculated from experimental data (black) and the best-fit simulations (dark yellow). LCoC (inter-interval distance at CoC = 0.5) = LBF (interference distance L for simulation) = 0.30 μm for both chromosomes XV and III. Error bar, SEM of the repeat experiments (B, D); data (n = 3; >200 nuclei for each experiment), simulation (n = 20; 5000 bivalents in each simulation).

other DNA double-strand (the transported-segment or T-segment) through the gap, and then religate the break (Supplementary Figure S1) (31–33). Mapping Zip3 foci on chromosome XV in different *top2* alleles affecting different steps of the strand-passage reaction showed three types of CO phenotypes (Figures 2, 3, Supplementary Figures S1, S2, and Table S3). Mutants (*top2-G738D* and *top2-P824S*) predicted to have a slow strand-passage reaction showed WT level of Zip3 foci (Type I; Figure 2A and Supplementary Table S3) (32,49). Mutants expressing *top2* alleles without DNA binding ability (*top2-K651A*) showed an increased number of Zip3 foci as with strains of Top2 depletion (P_{CLB2}-*TOP2*) or expressing catalytically inactive Top2 (*top2-Y782*F) (Type II; Figure 2A, Supplementary Figure S2 and Table S3) (21,50,51). However, mutants expressing *top2* alleles, which can cleave DNA but cannot complete the strand-passage reaction to release the religated DNA (*top2-L475A/L480P* (hereafter *top2-L475A*), *top2-G144I,* and *top2-E66Q*), showed a decreased number of Zip3 foci (Type III; Figure 2A and Supplementary Table S3) (52–54). Strains treated with topoisomerase inhibitors etoposide or ICRF-193, which separately inhibits G-segment religation after T-segment transport or DNA release, showed a similarly decreased number of Zip3 foci like Type III mutants (thus grouped to Type III mutants; Figure 2A and Supplementary Table S3). This is also consistent with a previous report that mouse spermatocytes showed a decreased number of COs after being treated with etoposide (55). Quantitative simulations also successfully captured corresponding alterations in Zip3 focus number in these three types of *top2* mutants (Figure 2B, Supplementary Figure S3, and Table S3; Materials and Methods).

CO interference restricts CO numbers, and stronger (weaker) CO interference leads to fewer (more) COs. Previously, we have shown increased CO number in *top2* depletion and catalytically inactive mutants results from decreased CO interference (21). The CoC curve analysis showed Type II mutants with increased numbers of Zip3 foci had decreased CO interference: the CoC curve was shifted to the left and L_{CoC} decreased from 0.3 to 0.25 μm (Figure 2C and Supplementary Table S3). In contrast, the CoC curve was shifted to the right and L_{CoC} increased from 0.3 to 0.35 μm, suggesting increased CO interference in Type III mutants with decreased numbers of Zip3 foci (Figure 2C and Supplementary Table S3). As expected, Type I mutants with WT level of Zip3 foci also showed WT level of interference (Figure 2A, C, and Supplementary Table S3). Alterations in Zip3 foci and CO interference in these mutants were further confirmed by quantitative simulations (Figure 2B, D, Supplementary Figure S3, and Table S3; Methods).

Three types of *top2* alleles with different CO interference and Zip3 focus numbers were confirmed by the same analysis on chromosome III in representative alleles (Figure 3A–D and Supplementary Table S4). This is consistent with the previous report that Top2 affects CO interference similarly

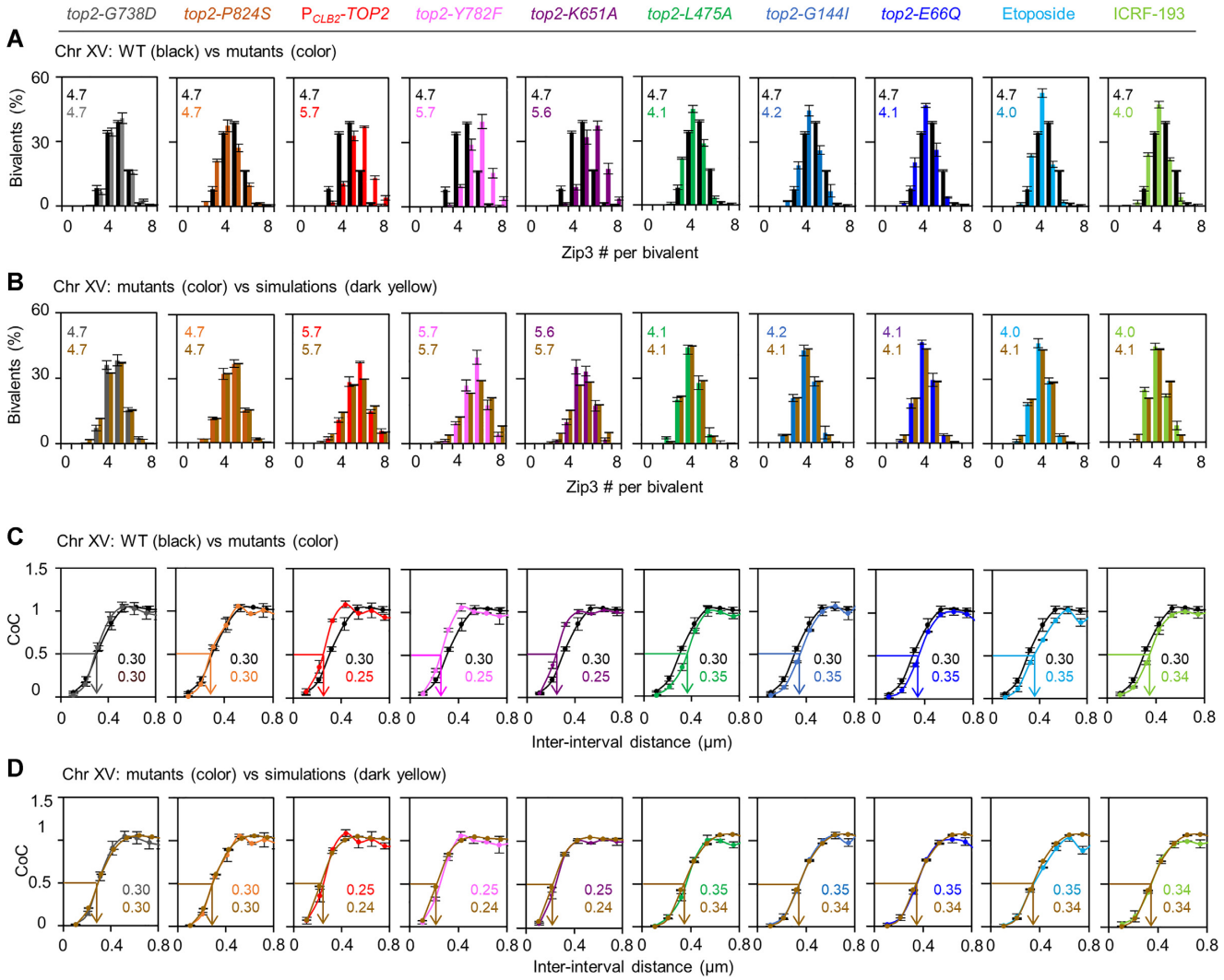

Figure 2. CO patterns on chromosome XV in top2 mutants. (**A**) Distribution of the numbers of Zip3 foci on chromosome XV (5–6h in SPM) in different strains (color) compared with WT (black). The average number of COs was shown at the top of each graph. (**B**) Distribution of simulated (dark yellow) CO numbers on chromosome XV compared with corresponding experimental data. The average number of COs was shown at the top of each graph. (**C**) Coefficient of coincidence analysis on chromosome XV in WT (black) and mutants (color). (**D**) The best-fit simulation of coefficient of coincidence on chromosome XV in mutants. LCoC and LBF were indicated (C and D). Dark yellow, simulations; other color, data. The color code for each strain was indicated at the top of the figure. Error bar, SEM of the repeat experiments (A–D); data ($n = 3$; >200 nuclei for each experiment), simulation ($n = 20$; 5000 bivalents in each simulation). WT data, duplicated from Figure 1. The data for CoC analysis were from Supplementary Table S3 in (A-D).

on both long and short chromosomes although very short chromosomes tend to have a higher DSB density (15,21,56). Corresponding alterations in the Zip3 focus number at the per-nucleus level were also observed (Figure 3E). Examination of the number of recombination intermediate Msh4 foci, which is believed to also mark CO sites in yeast meiosis, in representative *top2* alleles further confirmed the alterations in Zip3 focus number (57) (Supplementary Figure S4A, B). However, the number of Rad51 foci, which mark DSBs, was not affected in either the DMC1 or *dmc1*Δ backgrounds (Supplementary Figure S4C, D), suggesting that the DSB level is not significantly changed, which is consistent with a recent report that Top2 inactivation does not affect DSB level (58). The lengths of chromosome axes that regulate the number of COs were not altered in *top2* alleles (Supplementary Figure S5A, B). These results, in combination with our quantitative simulations, further support the idea that alterations in CO number in *top2* mutants result from altered CO interference but not DSB number (Supplementary Figure S6).

CO interference in these strains was further examined by two other approaches, modified CoC (MCoC) and gamma distribution (Methods). Similar to CoC analysis, for MCoC analysis, chromosomes are divided into multiple intervals to determine whether the existence of a CO in one interval reduces the CO frequency in another interval (21). A gamma distribution, which best describes the frequency distribution of distances between adjacent COs, is often used to define the interference strength. The assumption is that a larger shape parameter (γ) means stronger interference, although this method has intrinsic defaults (21,37). Both types of analyses confirmed that Type II and III mutants

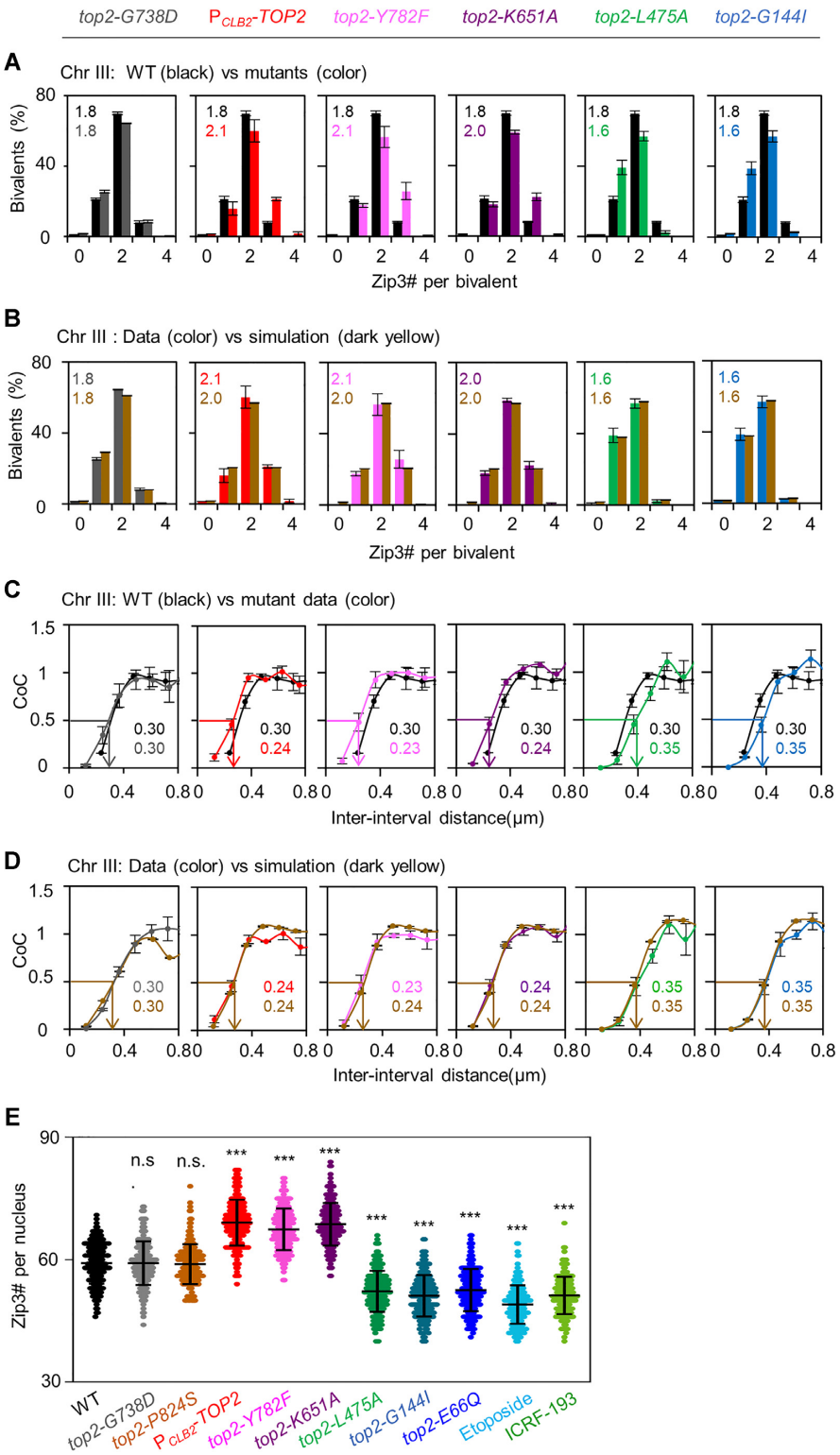

Figure 3. CO patterns on chromosome III and CO number per nucleus in top2 mutants. (**A**) Distribution of the numbers of Zip3 foci on chromosome III in WT (black) and mutants (color). The average number of COs was shown at the top of each graph. (**B**) Distribution of simulated (dark yellow) CO numbers on chromosome III compared with corresponding experimental data (color). The average number of COs was shown at the top of each graph. (**C**) Coefficient of coincidence analysis on chromosome III in WT (black) and mutants (color). (**D**) The best-fit simulation of coefficient of coincidence on chromosome III. LCoC and LBF were indicated. Dark yellow, simulations; other color, data. The color code for each strain was indicated at the top of the figure. Error bar, SEM of the repeat experiments (A–D); data ($n = 3$; >200 nuclei for each experiment), simulation ($n = 20$; 5000 bivalents in each simulation). WT data, duplicated from Figure 1. (**E**) The number of Zip3 foci per nucleus (5–6h in SPM). Error bar, SD. $n = 217$, 218, 225, 190, 207, 201, 222, 200, 199, 226, and 197 nuclei, respectively. n.s., not significant ($P > 0.05$); ***$P < 0.001$; Student's t-test. The data for CoC analysis were from Supplementary Table S4 in (A–D).

had decreased and increased interference, respectively, however, Type I mutants showed normal interference (Figure 4A–C, Supplementary Figure S7A, B, Tables S3 and S4).

Previously, in Top2 depletion and catalytically inactive mutants, we failed to distinguish the difference between increased strength of CO designation (that designates a recombination intermediate to be a CO) from the decreased CO interference both of which affect CO patterns very similarly (21). Here, in Type III mutants with decreased number of COs, we showed that a decrease in CO number in these mutants probably resulted from increased CO interference but not decreased CO-designation strength. This is because increased CO interference would not significantly alter the frequency of chromosomes without any COs, which is consistent with the observations in Type III mutants. However, decreased CO-designation strength would significantly increase the frequency of chromosomes without any COs (Supplementary Figure S6B).

Our earlier study showed that the meiosis-specific Top2 depletion mutant had decreased CO interference and consequently decreased CO homeostasis (21). CO homeostasis in Type III mutants was further examined in a series of strains with different frequencies of meiotic DSBs as previously described (21,28). Consistently, Type III mutants with increased CO interference showed increased CO homeostasis (Figure 4D). The alterations in CO homeostasis were also supported by quantitative simulations (Figure 4D). These results further confirm that the strength of CO homeostasis depends on the strength of CO interference as previously proposed (15,30).

Our above findings suggest that DNA cleavage by topoisomerases probably is required for efficient generating or spreading of CO interference, and cleaved DNA has to be re-ligated and released from Top2 to prevent over-accumulating or over-spreading of CO interference. Therefore, proper CO interference and thus CO number requires Top2 to timely complete the strand-passage reaction.

DNA supercoiling regulates CO interference

Yeast Top2 removes accumulated DNA catenation and negative supercoils via strand-passage reaction. However, it is unclear which function or both is required for proper CO interference. Bacteria have four topoisomerases that have different roles in regulating DNA catenation and supercoils (31,59). Each of the four topoisomerases and yeast Top2 was separately introduced into WT and the P_{CLB2}-*TOP2* mutant to change the levels of DNA catenation and/or supercoils (Figure 5A and Supplementary Figure S8). The ectopic expression of bacterial topoisomerases in these yeast strains did not change the expression of yeast Top2 and the introduction of extra copies of yeast Top2 increased the overall expression level of Top2 (Supplementary Figure S9).

Yeasts with extra copies of Top2 showed decreased number of Zip3 foci and increased CO interference, which is similar to the phenotypes of Type III mutants. Bacterium Topo I (TopA) can remove negative DNA supercoils (60). Yeasts expressing this topoisomerase showed decreased numbers of Zip3 foci and increased interference as with Type III mutants (Figure 5B-D and Supplementary Table S5). However, bacterium Topo II (gyrase) can introduce negative DNA supercoils (61), and yeast expressing this topoisomerase showed an increased number of Zip3 foci and decreased interference as with Type II mutants (Figure 5B–D and Supplementary Table S5). Bacterium Topo III (TopB) and Topo IV (ParC and E complex) can hardly remove negative supercoil and yeast expressing either one showed WT level of Zip3 number and interference (Figure 5B–D and Supplementary Table S5) (62,63). These results suggest that topoisomerases probably regulate CO interference and consequently CO number via modulating the level of DNA supercoils.

As expected, the defects of P_{CLB2}-*TOP2* were rescued by ectopically expressing Top2 (Figure 5B, E, F, and Supplementary Table S6). And consistent with the above prediction, the increased number of Zip3 foci and decreased CO interference in P_{CLB2}-*TOP2* were rescued to WT levels when bacterium Topo I was ectopically expressed which is predicted to remove accumulated negative DNA supercoils (Figure 5B, E, F, and Supplementary Table S6). The P_{CLB2}-*TOP2* mutant expressing bacterium Topo II, which is predicted to introduce more negative DNA supercoils and thus more COs and weaker interference, did not show a further increase in CO number or decrease in CO interference (Figure 5B, E, F and Supplementary Table S6). This may be due to the P_{CLB2}-*TOP2* mutant having already accumulated a high level of negative DNA supercoils and ectopically expressing bacterium Topo II in this mutant could not further increase the level of negative supercoils (below).

Our above results support the hypothesis that yeast Top2 regulates CO interference and thus CO number via modulating negative supercoils (Figure 5G, Supplementary Tables S5 and S6). Consistently, alterations in Top2 abundance gradually changed the strength of CO interference and correspondingly the frequency of COs (Figure 6, Supplementary Figure S10, S11, and Table S7). This, in combination with the role of strand-passage reaction in regulating interference, supports the idea that the accumulation and relief of negative supercoils decrease and increase the strength of interference, respectively.

Negative supercoils preferentially accumulate at CO-associated regions independent of the occurrence of DSBs

Our above results support the hypothesis that DNA negative supercoils regulate CO interference. The level of negative supercoils is proportional to and thus can be measured by the level of the intercalation of psoralen into DNA (39,64). The genome-wide negative supercoils were mapped using biotinylated TMP (4,5′,8-trimethylpsoralen; bTMP) in WT (Type I) and two representative *top2* alleles (P_{CLB2}-*TOP2* for Type II and *top2-L475A* for Type III) (Figure 7, Supplementary Figures S12 and S13). For each strain, the experiment was done with samples separately collected at 3, 4 and 5 h in SPM and with two biological repeats. The ChIP-seq results of the two repeats for each strain at each time point showed a strong correlation ($r > 0.9$) (Supplementary Figure S12). From 3–5 h in SPM, the distribution and level of detected negative supercoils were highly stable and showed strong correlations for each strain between different time points, suggesting the level of negative supercoils is maintained constantly during this period (Supplementary Figures S12 and S13). Therefore, the data from 4h samples of the first experiment were used for further analysis.

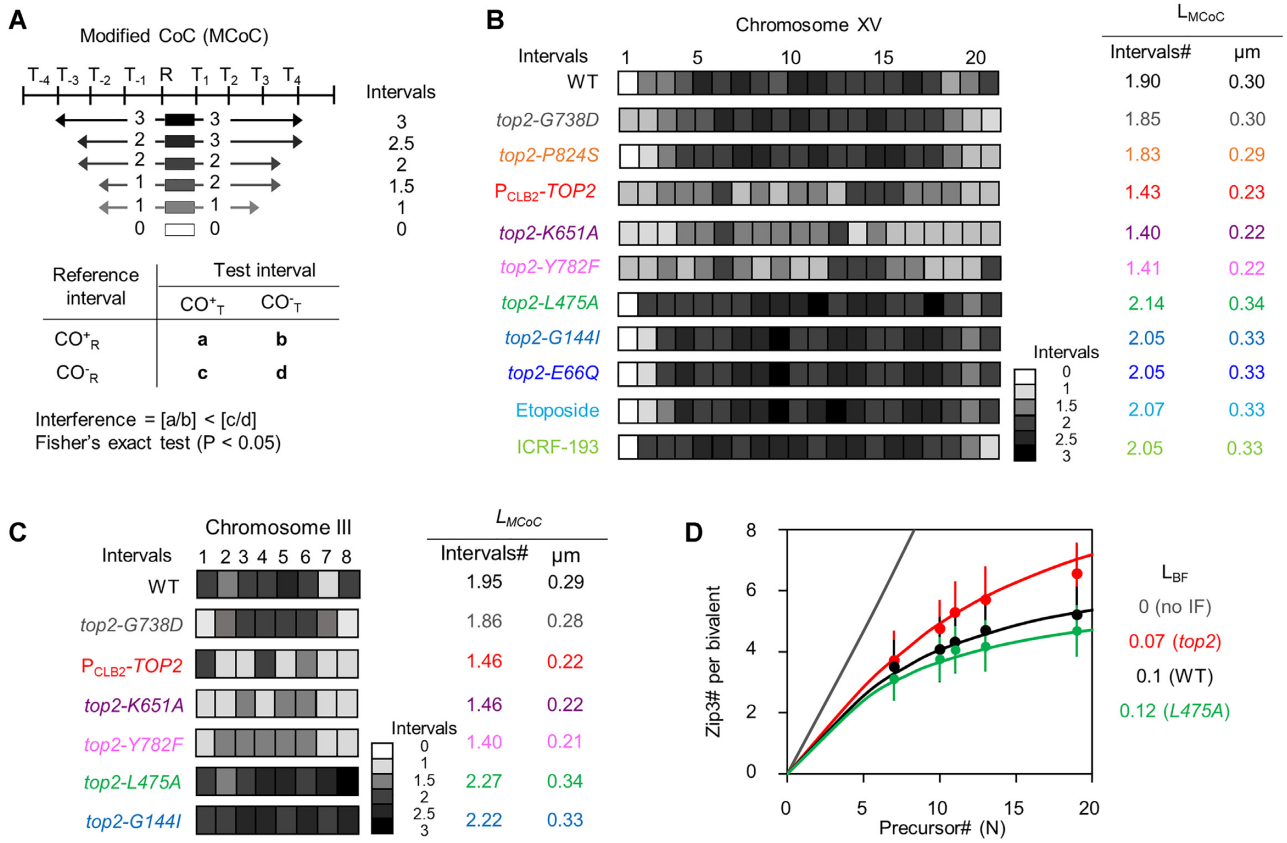

Figure 4. Analysis of CO interference by MCoC and CO homeostasis. (**A**) Illustration of the MCoC approach (Methods). (**B**) Analysis of CO interference on chromosome XV by MCoC. (**C**) Analysis of CO interference on chromosome III by MCoC. (**D**) Quantitative analysis of crossover homeostasis for WT and mutants on chromosome XV. Compared with WT (black), mutants with increased CO interference had increased strength of CO homeostasis (green), however, mutants with decreased CO interference had decreased strength of CO homeostasis (red). Grey, predicted curve for absent CO interference (i.e. $L = 0$). Curve, the relationship between the numbers of Zip3 foci and precursors (N) predicted by simulations; dot, the number of Zip3 foci detected in strains with different DSB levels in *TOP2* (red), P_{CLB2}-*TOP2* (black), and *top2-L475A* (green) backgrounds on chromosome XV. Error bar, SD. $n = 228$, 197, 100, 243 and 204 nuclei for WT; 135, 175, 158, 143 and 169 nuclei for P_{CLB2}-*TOP2*; 198, 199, 211, 211 and 197 nuclei for *top2-L475A*, in a series of strains with different levels of DSBs (*spo11-Y135F/spo11-HA*, *spo11-D290A/spo11-HA*, *spo11-HA/spo11-HA*, *SPO11/SPO11*, and *tel1*△). WT and P_{CLB2}-*TOP2* data in (D), from (21). The data for MCoC analysis were from Supplementary Table S3 (B) and S4 (C).

Since genome-wide ChIP-seq data for Top2 and DSB/recombination-related markers are publicly available (Methods), their relationships with negative supercoils were further examined. As expected, 90% of Top2 binding regions showed enrichment of negative supercoils, and 50% of negative supercoil-rich regions also had Top2 binding. Importantly, negative supercoils enriched at Spo11 oligo-defined DSB hotspots and CO-associated Zip3 binding regions (Figure 7A, B). Moreover, regions with low, medium, and high levels of Top2 tended to have low, medium, and high levels of negative supercoils, respectively (Figure 7C, left). Similarly, regions with low, medium, and high levels of negative supercoils also tended to have low, medium, and high levels of Top2 binding, respectively (Figure 7D, left). The same relationships were also observed between negative supercoils and Spo11 oligo-defined DSB hotspots and Zip3 binding regions (Figure 7C, D). Additionally, regions with more Zip3 binding tended to have more negative supercoils enriched at the center of Zip3 peaks (Figure 7C). However, regions with less Zip3 binding tended to have fewer negative supercoils, and the negative supercoils were located at one (60%) or both (30%) sides of Zip3 peaks (Figure 7C). This result is consistent with the idea that negative supercoils regulate the formation of Zip3 foci (COs) and thus regions with more negative supercoils may tightly restrict the CO to the center, however, regions with less negative supercoils have less power in controlling the formation and the position of COs.

Enrichment of negative supercoils at recombination-associated Zip2, Zip4 and Msh5 binding regions was also observed as at Zip3 binding regions (Supplementary Figure S14A-C). Consistently, the levels of negative supercoils were strongly correlated with Zip2, Zip3, Zip4 and Msh5 (Supplementary Figure S14D). However, their enrichment at regions for Mer2, Rec114 and Spp1 (required for efficient DSB formation) was not obvious (Supplementary Figure S14E–G). And the levels of negative supercoils were only weakly/moderately correlated with Mer2, Rec114 and Spp1 (Supplementary Figure S14H). This is because DSB and recombination sites locate at chromatin loops, however, Spp1 and RMM complex (Rec114, Mer2 and Mei4) locate at chromosome axes (Supplementary Figure S14J–M; (65,66)). Furthermore, when regions with negative supercoils were divided into regions with Zip3 binding (representing CO sites), regions enriched with Spo11 oligos but

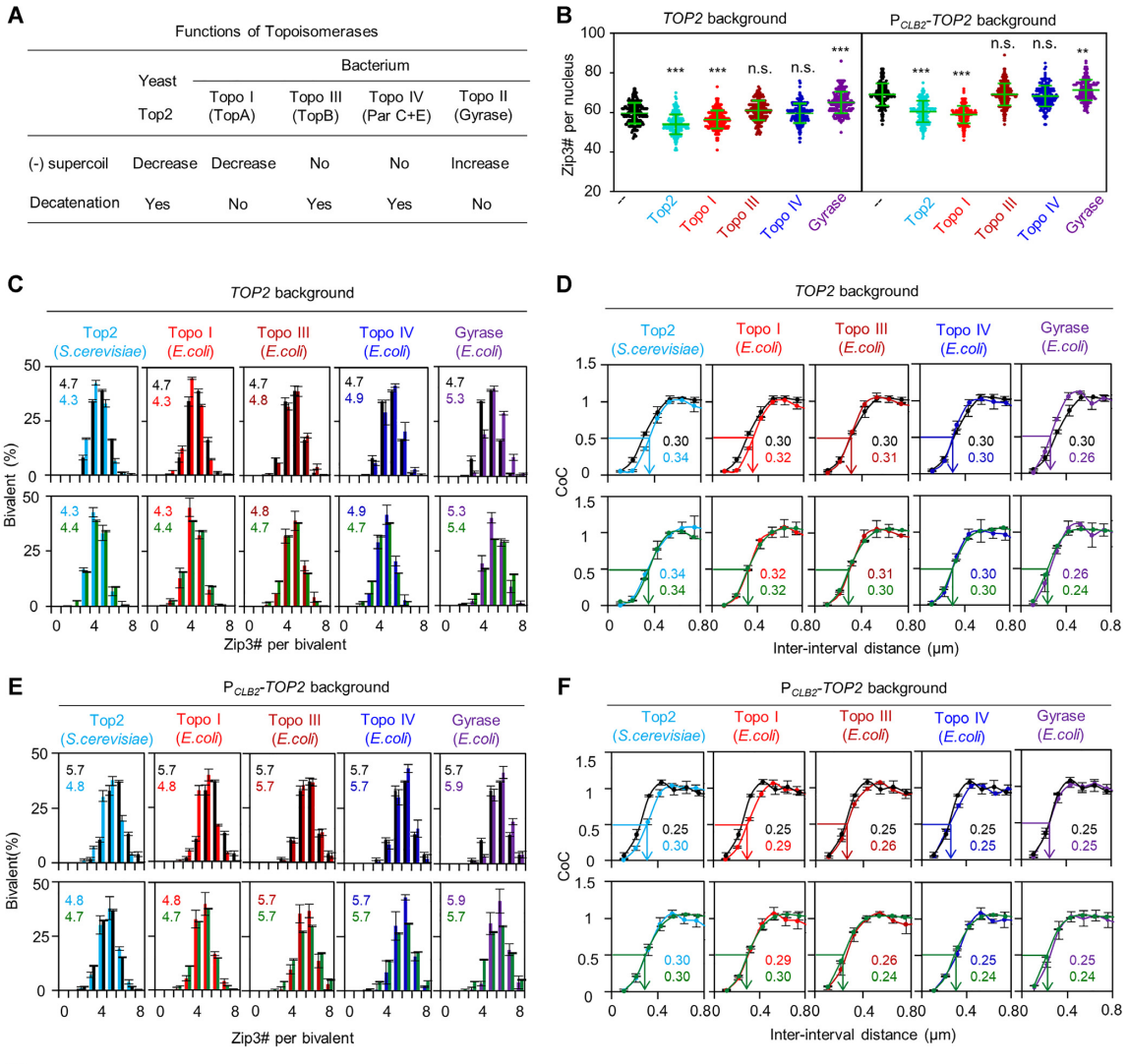

	Yeast	Bacterium			
	Top2	Topo I (TopA)	Topo III (TopB)	Topo IV (Par C+E)	Topo II (Gyrase)
(-) supercoil	Decrease	Decrease	No	No	Increase
Decatenation	Yes	No	Yes	Yes	No

G Effects of *E.coli* Topoisomerases in yeast meiosis

	TOP2						P_{CLB2}-*TOP2*					
	—	Top2	Topo I	Topo III	Topo IV	Gyrase	—	Top2	Topo I	Topo III	Topo IV	Gyrase
(-) supercoil	—	↓	↓	—	—	↑	↑	↓	↓	—	—	↑
Catenated DNA	—	↓	—	↓	↓	—	↑	↓	—	↓	↓	—
ChrXV Zip3#	4.7	4.3	4.4	4.7	4.8	5.1	5.7	4.7	4.7	5.7	5.7	6.0
Nucleus Zip3#	59.7	54	56.5	61.2	59.6	64.3	69.8	60.1	59.2	68.9	68.3	71.3
Interference (μm)	0.30	0.34	0.32	0.31	0.30	0.26	0.25	0.30	0.29	0.26	0.25	0.25

Figure 5. TopoII's supercoiling activity is related to CO interference. (**A**) Functions of DNA topoisomerases in DNA decatenation and supercoils. (**B**) COs number per nucleus in yeast expressing different topoisomerases in either *TOP2* (left part) or P_{CLB2}-*TOP2* (right part) background. n = 197, 184, 202, 209, 221 and 210 nuclei in *TOP2* background; 190, 234, 213, 227, 231 and 203 nuclei in P_{CLB2}-*TOP2* background. Error bar, SD. n.s. (not significant), $P > 0.05$; $^{**}P < 0.05$; $^{***}P < 0.001$, compared with the *TOP2* (left part) or P_{CLB2}-*TOP2* (right) control. Student's *t*-test. (**C**) CO number distributions on chromosome XV in strains expressing different topoisomerases compared with WT (black, top panel) and best-fit simulations (green, bottom panel) in *TOP2* background. The average number of COs was indicated. (**D**) CoC curves on chromosome XV in strains expressing different topoisomerases compared with WT (black, top panel) and best-fit simulations (green, bottom panel) in TOP2 background. LCoC and LBF were indicated. (**E**) CO number distributions on chromosome XV in strains expressing different topoisomerases compared with P_{CLB2}-*TOP2* (black, top panel) and best-fit simulations (green, bottom panel) in P_{CLB2}-*TOP2* background. The average number of COs was indicated. (**F**) CoC curves on chromosome XV in strains expressing different topoisomerases compared with P_{CLB2}-*TOP2* (black, top panel) and best-fit simulations (green, bottom panel) in P_{CLB2}-*TOP2* background. L_{CoC} and L_{BF} were indicated. Error bar, SEM of the repeat experiments (C–F); data (three independent experiments and > 200 nuclei for each experiment), simulation (n = 20; 5000 bivalents in each simulation). n.s., not significant ($P > 0.05$); $^{**}P < 0.05$; $^{***}P < 0.001$. Student's *t*-test. WT data, duplicated from Figure 1; P_{CLB2}-*TOP2* data, duplicated from Figure 2. (**G**) Effects of ectopically expressed different topoisomerases on meiotic recombination. Samples were collected at 5–6 h in SPM (B–F). The data for CoC analysis were from Supplementary Table S5 (C, D) and S6 (E, F).

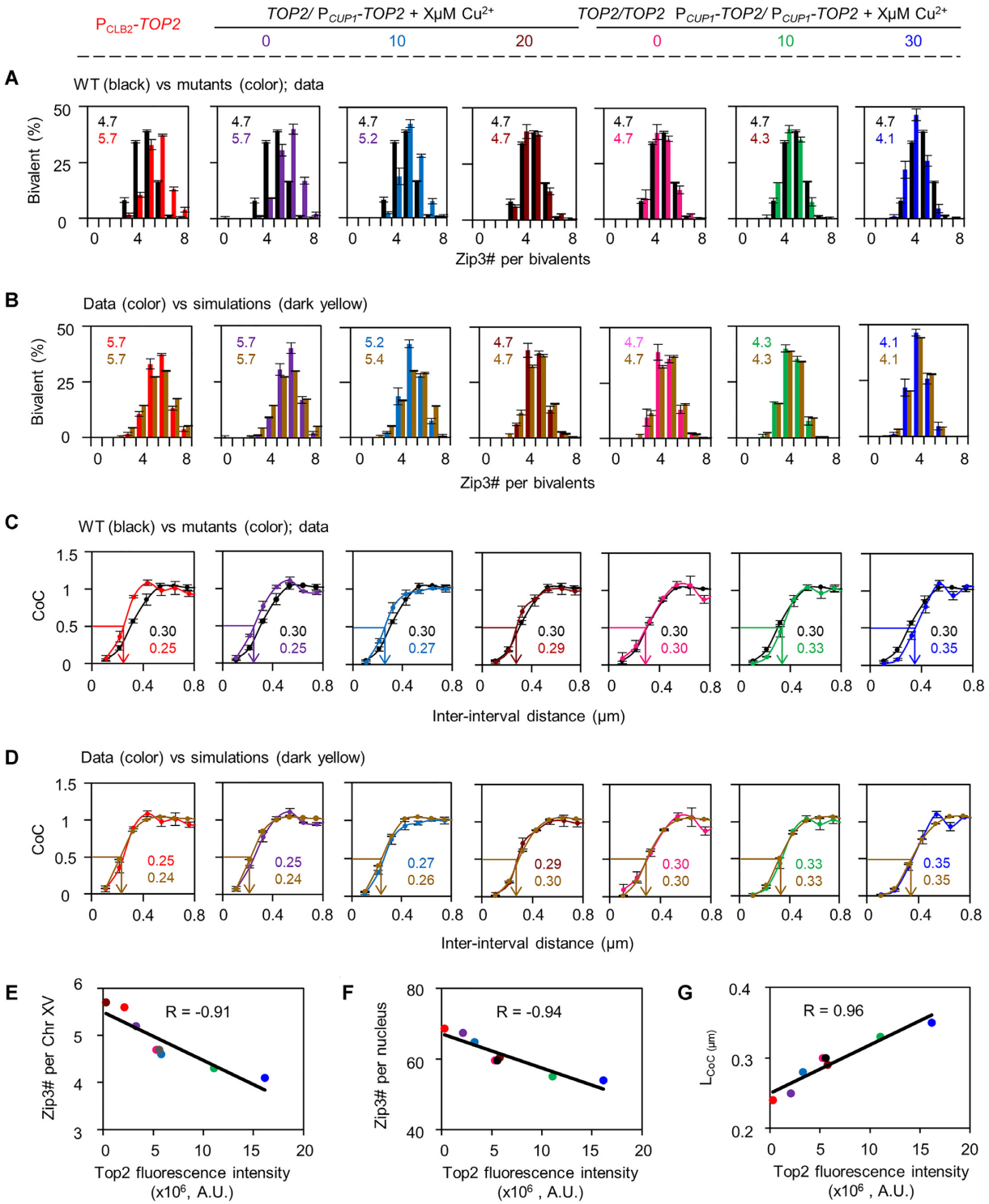

Figure 6. Top2 regulates CO interference and CO frequency in a dosage-dependent manner. *TOP2*/P_{CUP1}-*TOP2* strain (the native promoter of one copy of *TOP2* was replaced by the *CUP1* promotor) and *TOP2*/ *TOP2* P_{CUP1}-*TOP2*/ P_{CUP1}-*TOP2* strain (two copies of P_{CUP1}-*TOP2* were integrated into the genome) were treated with different concentrations of Cu^{2+} as indicated on the top of the graph. (**A, B**) Distribution of the numbers of Zip3 foci (A) and simulated COs (B) on chromosome XV. (**C, D**) CoC curves from experimental data (C) and the best-fit simulations (D) on chromosome XV. Cells were collected from the synchronized culture at 5 h in SPM (A–D). Error bar (A–D), range of 2 experiments (data) or SEM for simulations ($n = 20$; 5000 bivalents for each simulation). (**E**) The correlation between the average numbers of Zip3 foci on chromosome XV (data from panel A) and the fluorescence intensity of Top2. (**F**) The correlation between the average numbers of Zip3 foci per nucleus and the fluorescence intensity of Top2. (**G**) The correlation between the CO interference (L_{CoC}) (data from panel C) and the fluorescence intensity of Top2. The data for Top2 fluorescence intensity in panels E-G were from Supplementary Figure S10. Color keys were indicated on the top of the graph. R, Pearson's correlation coefficient (E-G). WT data, duplicated from Figure 1; P_{CLB2}-*TOP2* data, duplicated from Figure 2. Strains (E-G): P_{CLB2}-*TOP2*, *TOP2*/P_{CUP1}-*TOP2* with 0, 10 and 20 μM Cu^{2+}; WT, *TOP2*/ *TOP2* P_{CUP1}-*TOP2*/ P_{CUP1}-*TOP2* with 0, 10 and 30 μM Cu^{2+}. The data for CoC analysis were from Supplementary Table S7 in (A–D).

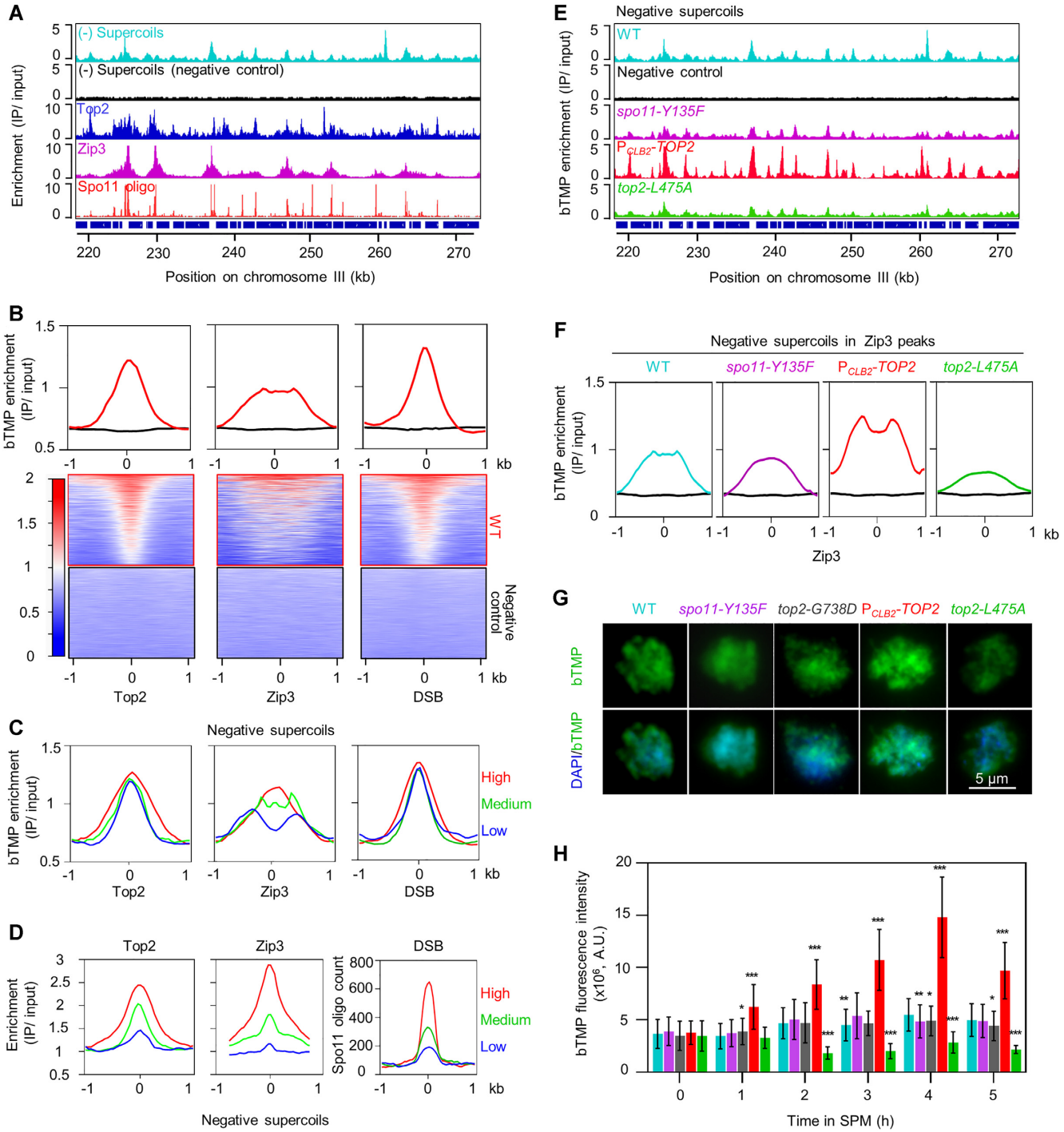

Figure 7. DNA negative supercoils preferentially enrich at CO sites. (**A**) An integrative genomics viewer illustration of DNA negative supercoils, Top2, Zip3 and Spo11 oligos (measuring DSBs) enrichment (4 h in SPM) in a segment of chromosome III. (**B**) The averaged profiles (top) and heatmaps (bottom) of DNA negative supercoil enrichment within ±1 kb at Top2 peaks (left), Zip3 peaks (middle), and DSB hotspots (defined by Spo11 oligos; right) identified by ChIP-seq in WT (red) and the negative control (black) (4 h in SPM). (**C**) As in (B) but peaks of Top2, Zip3, and DSB hotspots were divided into 3 groups according to ChIP-seq read number (low, blue; medium, green; high, red). (**D**) Analog to (C) to show the enrichments of Top2, Zip3, and Spo11 oligos at the regions with low (blue), medium (green), and high (red) levels of negative supercoils. (**E**) As in (A) to show enrichment of DNA negative supercoils in WT, *spo11-Y135F* (eliminating DSBs and recombination), P_{CLB2}-*TOP2* and *top2-L475A* (4 h in SPM) in a segment of chromosome III. (**F**) As in (B) to show enrichment of DNA negative supercoils (4 h in SPM) at Zip3 peaks in WT, *spo11-Y135F*, P_{CLB2}-*TOP2* and *top2-L475A*. Negative supercoils at Zip3 peaks in the negative control (black) were indicated on each graph (A–F). (**G**) Representative images to show DNA negative supercoils in surface-spread meiotic nuclei by immunostaining (4 h in SPM). Cells were treated with bTMP and stained with neutravidin. Scale bar, 5 μm. (**H**) Quantification of DNA negative supercoils in (G). Error bar, SD. From left to right, n = 92, 114, 51, 99 and 108 nuclei (0 h in SPM); 106, 72, 52, 77 and 68 nuclei (1 h); 76, 59, 47, 89 and 144 nuclei (2 h), 73, 116, 64, 73 and 120 nuclei (3 h), 78, 87, 62, 88 and 182 nuclei (4 h), 82, 51, 64, 63 and 87 nuclei (5 h). *$P < 0.05$; **$P < 0.01$; ***$P < 0.001$; Student's *t*-test. Only those with a statistical difference were indicated.

the absence of Zip3 binding (representing NCO sites), and regions absence of Spo11 oligos (representing DSB cold spots), CO sites tended to have more negative supercoils, however, NCO sites and DSB cold spots had less and very similar levels of negative supercoils (Supplementary Figure S14I). These results support the idea that regions with more negative supercoils tend to accumulate more CO-associated molecules for CO formation.

Further investigations in representative *top2* mutants (*top2-G738D,* P_{CLB2}*-TOP2* and *top2-L475A*) showed the three types of alleles had WT, increased, and decreased levels of negative supercoils, respectively, as expected (Figure 7E–H and Supplementary Figure S13). Moreover, increased and decreased levels of negative supercoils were also observed in yeasts expressing bacterium Topo II and Topo I, respectively, in both *TOP2* and P_{CLB2}*-TOP2* backgrounds, which is consistent with the altered levels of CO interference and number of Zip3 foci (Supplementary Figures S15 and S16). Yeasts expressing bacterium Topo III and Topo IV showed little alterations in interference strength and Zip3 focus number and also little alterations in negative supercoil level (Supplementary Figure S16).

Our above results showed that the level of negative supercoils was highly correlated with the enrichment of Zip3. Moreover, this relationship was seen during DSB formation (∼3 h in SPM). However, there is also the possibility that the DSB- and/or Zip3-related events cause the accumulation of negative supercoils. To exclude this possibility, we further examined the negative supercoils in a *spo11-Y135F* strain, where DSB formation and thus CO formation is eliminated. In this strain, the distribution and enrichment of negative supercoils were comparable to that in WT (Figure 7E–H and Supplementary Figure S17). This result suggests that the accumulation of DNA negative supercoils is independent of DSB formation and occurs before CO formation. Therefore, our results support the idea that negative supercoils regulate CO interference and CO formation and preferentially accumulate in regions that tend to form COs.

DISCUSSION

Negative supercoils regulate meiotic crossover patterns

A lot of effort has been made to identify the signal of CO interference and several models have been proposed to interpret CO interference although few are supported by enough evidence [e.g. (25,67–69)]. We previously proposed that CO interference involves accumulation, relief, and redistribution of mechanical stress (15,21). Our current findings suggest that DNA negative supercoil is the possible mechanical stress and thus further support this hypothesis.

(1) Yeast strains accumulating more negative supercoils have weaker CO interference and more COs. Similarly, yeasts accumulating less negative supercoils have stronger CO interference and fewer COs (Figures 2–5, Supplementary Tables S3–S6). Consistently, yeasts expressing more (less) Top2 and thus predicted to have less (more) negative supercoils tend to have stronger (weaker) CO interference and fewer (more) COs (Figure 6 and Supplementary Table S7).
(2) Yeast top2 mutants that cannot cleave DNA (e.g. alleles cannot bind on chromosomes or absence of the enzyme activity) accumulate more negative supercoils and show weaker interference. Yeast top2 mutants that cannot re-ligate cleaved DNA or release the re-ligated DNA prevent the re-accumulation of negative supercoil and show stronger interference (Figures 2–4, 7 and Supplementary Tables S3 and S4).
(3) DNA negative supercoils are preferentially enriched in CO regions but less so in NCO regions and regions with more negative supercoils tend to accumulate more CO-associated molecules (Figure 7). Importantly, DNA negative supercoils are accumulated to a high level independent of DSB formation and before CO designation at zygotene (∼4 h in SPM) (Figure 7).

How do DNA negative supercoils regulate CO interference? Accumulation of DNA negative supercoils can directly result in local strand separation and chromatin expansion and cause chromatin at a state with high stress. The local alterations could also be spread outwards and result in alterations in the DNA/chromatin state at a large scale (43,52,70). These alterations either locally or at a large scale can disturb the axis state/continuity and thus affect CO interference spreading speed/distance or CO designation. Top2 works on chromosome axes to regulate the mechanical property of chromosomes has also been suggested in mammal mitotic nuclei [e.g. (71)]. These effects could be achieved either directly by DNA/chromatin changes or indirectly, e.g. by changing histone modifications, DNA-protein interactions, or protein-protein interactions involved in these processes. Similar effects are known in transcription and replication (72–74). Therefore, the level of DNA negative supercoils has to be well regulated mainly by topoisomerases to maintain chromatin at a proper stress level and thus CO interference strength and CO numbers during meiotic recombination.

Under the above scenario, when the negative supercoil and thus the mechanical stress for CO designation is accumulated to a higher level, e.g. in the absence of Top2, more COs occur. Consistently, negative supercoils have been suggested to promote strand invasion and Holliday junction formation during homologous recombination (75–77). When negatively supercoiled DNA is cleaved, the negative supercoil and thus the stress is released. Early studies showed that Dmc1 can interact with and activate Top2, meanwhile, Top2 inhibits Dmc1-dependent strand transfer activity in *Coprinus cinereus* (78,79). We propose that this probably occurs after CO designation and the predicted consequence for these effects would be the relaxation of negative supercoils and a decrease in the probability of CO formation. The cleaved DNA fragments have to be timely re-ligated to maintain negative supercoils at a proper level. Otherwise, if negative supercoil is released to a very low level or cannot re-accumulate to a proper level, fewer COs would be formed as observed in Type III *top2* mutants. Consistently, increased or decreased amounts of topoisomerases working on supercoils could disrupt this balance and lead to increased or decreased interference (and thus decreased or increased numbers of COs), respectively (Figure 6 and Supplementary Table S7).

Changing negative supercoils can have multiple consequences on DNA metabolism including chromatin organization and gene expression (80–82). It is also possible that

these changes may directly or indirectly impact CO interference and CO number.

Although our current result fit the stress model, it does not exclude other models of CO interference. A promising one is the recently proposed diffusion-mediated coarsening model (83). In this model, a large number of small HEI10 foci diffuse along the synaptonemal complex (between a pair of homologous chromosome axes at pachytene) and undergo competitive coarsening to form a small number of large HEI10 foci (labeling CO sites), which are nearly evenly-spaced. Consistently, higher and lower HEI10 dosages result in weaker and stronger crossover interference, respectively (83). Negative supercoils could affect the diffuse/ coarsening process and/or absorb HEI10 to affect CO formation and interference. It is also possible that the mechanical stress may work with the coarsening mechanism and/or other mechanisms to robustly pattern COs during meiosis.

Do intrinsic genomic features dictate crossover distribution?

The distribution and level of negative supercoils in *spo11-Y135F* are comparable to that in WT. Moreover, a high level of negative supercoils accumulates before DSB formation (0–2 h in SPM) in meiotic cells (Figure 7G, H). These results indicate that negative supercoils largely accumulate before and independently of the occurrence of DSBs and recombination (Figure 7G, H and Supplementary Figure S17). This does not exclude the possibility that DSBs and recombination intermediates could also regulate negative supercoils, especially as we have proposed that CO designation could locally relieve negative supercoils to suppress further CO formation nearby (above). Negative supercoils tend to accumulate behind replication fork during DNA replication and RNA polymerase during transcription, and locate at promoter regions, which are often recombination hotspots (43,66). These considerations indicate that negative supercoils likely act as an intrinsic feature of the genome to dictate CO patterns. However, we cannot completely exclude the possibility that these different processes are simply independent and happen to correlate in space.

The idea that intrinsic genomic features dictate crossover distribution is also supported by recent studies. One study shows that CO surrounding regions have elevated interactions with their genomic neighborhoods and this feature persists through meiosis and seems to be independent of DSBs/recombination (84). Another study shows that COs tend to be located at DNA sequences with a higher GC-content and symmetric binding of Prdm9 (85). Consistently, the third study shows CO regions show more open chromatin states and are enriched with more Prdm9 mediated H3K4me3 (86). It is well known that these active and open chromatin regions tend to accumulate more negative supercoils (43,87). This likely explains why negative supercoils accumulate at the future CO sites and regulate CO patterns.

Negative supercoils are accumulated during many processes including DNA replication and transcription and these processes also require an optimal level of negative supercoils, e.g. negative supercoils favor strand separation (88–92). Therefore, the complete removal or accumulation of a very high level of negative supercoils is less likely in vivo. In this study, the level of negative supercoils is increased or decreased by ∼2 folds in various *top2* mutants (Figure 7H). This may explain why CO interference is only moderately altered in these *top2* mutants. Additionally, DSBs also show competition/interference and tend to be evenly spaced along any given chromosome (e.g. (93–96)). This also contributes to a base level of CO interference (15). As discussed above, negative supercoils may also work with other factors to regulate the interference and distribution of COs.

DATA AVAILABILITY

Data used in the paper are present in the paper and/or the Supplementary Materials. The bTMP ChIP-seq data are deposited at NCBI Gene Expression Omnibus (GEO) database under accession number GSE201366. Other ChIP-seq data were downloaded from GEO or SRA with the following accession number: GSE103877 (Zip2, Zip3 and Zip4), GSE169760 (Top2), GSE67910 (Spo11 oligos), GSE119786 (Mer2), GSE119787 (REC114), GSE107967 (Spp1), GSE70112 (Red1 and Rec8), and SRP129066 (Msh5).

SUPPLEMENTARY DATA

Supplementary Data are available at NAR Online.

ACKNOWLEDGEMENTS

We thank Duncan J. Clark (University of Minnesota) for plasmids to make *top2* alleles; N. Kleckner (Harvard University) for discussions.

Author contributions: T.T., L.Z. and S.W., conceived of and designed the experiments. T.T., T.Y., Y.W., X.Y., B.Z., S.Z., X.Y., H.N., J.G. and J.Z. executed the experiments. T.T., L.Z. and S.W. analyzed the data and wrote the manuscript with inputs and edits from all authors.

FUNDING

National Natural Science Foundation of China [32070575, 31771385, 31801203, 31900402, 31890782]; Taishan Scholars Youth Project of Shandong Province. Funding for open access charge: National Natural Science Foundation of China.

Conflict of interest statement. None declared.

REFERENCES

1. Jones,G.H. and Franklin,F.C. (2006) Meiotic crossing-over: obligation and interference. *Cell*, **126**, 246–248.
2. Hunter,N. (2015) Meiotic recombination: the essence of heredity. *Cold Spring Harb. Perspect. Biol.*, **7**, a016618.
3. Gray,S. and Cohen,P.E. (2016) Control of meiotic crossovers: from double-strand break formation to designation. *Annu. Rev. Genet.*, **50**, 175–210.
4. Wang,S., Shang,Y., Liu,Y., Zhai,B., Yang,X. and Zhang,L. (2021) Crossover patterns under meiotic chromosome program. *Asian J. Androl.*, **23**, 562–571.
5. Shang,Y., Tan,T., Fan,C., Nie,H., Wang,Y., Yang,X., Zhai,B., Wang,S. and Zhang,L. (2022) Meiotic chromosome organization and crossover patterns. *Biol. Reprod.*, **107**, 275–288.
6. Keeney,S., Giroux,C.N. and Kleckner,N. (1997) Meiosis-specific DNA double-strand breaks are catalyzed by spo11, a member of a widely conserved protein family. *Cell*, **88**, 375–384.

7. Baudat,F., Manova,K., Yuen,J.P., Jasin,M. and Keeney,S. (2000) Chromosome synapsis defects and sexually dimorphic meiotic progression in mice lacking spo11. *Mol. Cell.*, **6**, 989–998.
8. Lichten,M. and de Massy,B. (2011) The impressionistic landscape of meiotic recombination. *Cell*, **147**, 267–270.
9. Lange,J., Yamada,S., Tischfield,S.E., Pan,J., Kim,S., Zhu,X., Socci,N.D., Jasin,M. and Keeney,S. (2016) The landscape of mouse meiotic double-strand break formation, processing and repair. *Cell*, **167**, 695–708.
10. Robert,T., Nore,A., Brun,C., Maffre,C., Crimi,B., Bourbon,H.M. and de Massy,B. (2016) The topovib-Like protein family is required for meiotic DNA double-Strand break formation. *Science*, **351**, 943–949.
11. McMahill,M.S., Sham,C.W. and Bishop,D.K. (2007) Synthesis-dependent strand annealing in meiosis. *PLoS Biol.*, **5**, e299.
12. Brown,M.S. and Bishop,D.K. (2014) DNA strand exchange and RecA homologs in meiosis. *Cold Spring Harb. Perspect. Biol.*, **7**, a016659.
13. Hunter,N. and Kleckner,N. (2001) The single-end invasion: an asymmetric intermediate at the double-Strand break to double-holliday junction transition of meiotic recombination. *Cell*, **106**, 59–70.
14. Ahuja,J.S., Harvey,C.S., Wheeler,DL. and Lichten,M. (2021) Repeated strand invasion and extensive branch migration are hallmarks of meiotic recombination. *Mol. Cell.*, **81**, 4258–4270.
15. Zhang,L., Liang,Z., Hutchinson,J. and Kleckner,N. (2014) Crossover patterning by the beam-film model: analysis and implications. *PLoS Genet.*, **10**, e1004042.
16. Pazhayam,N.M., Turcotte,C.A. and Sekelsky,J. (2021) Meiotic crossover patterning. *Front. Cell Dev. Biol.*, **9**, 681123.
17. von Diezmann,L. and Rog,O. (2021) Let's get physical - mechanisms of crossover interference. *J. Cell Sci.*, **134**, jcs255745.
18. Pyatnitskaya,A., Borde,V. and De Muyt,A. (2019) Crossing and zipping: molecular duties of the ZMM proteins in meiosis. *Chromosoma*, **128**, 181–198.
19. Agarwal,S. and Roeder,G.S. (2000) Zip3 provides a link between recombination enzymes and synaptonemal complex proteins. *Cell*, **102**, 245–255.
20. Fung,J.C., Rockmill,B., Odell,M. and Roeder,G.S. (2004) Imposition of crossover interference through the nonrandom distribution of synapsis initiation complexes. *Cell*, **116**, 795–802.
21. Zhang,L., Wang,S., Yin,S., Hong,S., Kim,K.P. and Kleckner,N. (2014) Topoisomerase II mediates meiotic crossover interference. *Nature*, **511**, 551–556.
22. Qiao,H., Prasada,R.H.B., Yang,Y., Fong,J.H., Cloutier,J.M., Deacon,D.C., Nagel,K.E., Swartz,R.K., Strong,E., Holloway,J.K. *et al.* (2014) Antagonistic roles of ubiquitin ligase HEI10 and SUMO ligase RNF212 regulate meiotic recombination. *Nat. Genet.*, **46**, 194–199.
23. Reynolds,A., Qiao,H., Yang,Y., Chen,J.K., Jackson,N., Biswas,K., Holloway,J.K., Baudat,F., de Massy,B., Wang,J. *et al.* (2013) RNF212 is a dosage-sensitive regulator of crossing-over during mammalian meiosis. *Nat. Genet.*, **45**, 269–278.
24. Zickler,D. and Kleckner,N. (2016) A few of our favorite things: pairing, the bouquet, crossover interference and evolution of meiosis. *Semin. Cell Dev. Biol.*, **54**, 135–148.
25. Morgan,C., White,M.A., Franklin,F., Zickler,D., Kleckner,N. and Bomblies,K. (2021) Evolution of crossover interference enables stable autopolyploidy by ensuring pairwise partner connections in arabidopsis arenosa. *Curr. Biol.*, **31**, 4713–4726.
26. Wang,S., Veller,C., Sun,F., Ruiz-Herrera,A., Shang,Y., Liu,H., Zickler,D., Chen,Z., Kleckner,N. and Zhang,L. (2019) Per-nucleus crossover covariation and implications for evolution. *Cell*, **177**, 326–338.
27. Veller,C., Kleckner,N. and Nowak,M.A. (2019) A rigorous measure of genome-wide genetic shuffling that takes into account crossover positions and mendel's second law. *Proc. Natl. Acad. Sci. U.S.A.*, **116**, 1659–1668.
28. Martini,E., Diaz,R.L., Hunter,N. and Keeney,S. (2006) Crossover homeostasis in yeast meiosis. *Cell*, **126**, 285–295.
29. Yokoo,R., Zawadzki,K.A., Nabeshima,K., Drake,M., Arur,S. and Villeneuve,A.M. (2012) COSA-1 reveals robust homeostasis and separable licensing and reinforcement steps governing meiotic crossovers. *Cell*, **149**, 75–87.
30. Wang,S., Zickler,D., Kleckner,N. and Zhang,L. (2015) Meiotic crossover patterns: obligatory crossover, interference and homeostasis in a single process. *Cell Cycle*, **14**, 305–314.
31. Wang,J.C. (2002) Cellular roles of DNA topoisomerases: a molecular perspective. *Nat. Rev. Mol. Cell Biol.*, **3**, 430–440.
32. Furniss,K.L., Tsai,H.J., Byl,J.A., Lane,A.B., Vas,A.C., Hsu,W.S., Osheroff,N. and Clarke,D.J. (2013) Direct monitoring of the strand passage reaction of DNA topoisomerase II triggers checkpoint activation. *PLoS Genet.*, **9**, e1003832.
33. Giménez-Abián,J.F., Lane,A.B. and Clarke,D.J. (2018) Analyzing mitotic chromosome structural defects after topoisomerase II inhibition or mutation. *Methods Mol. Biol.*, **1703**, 191–215.
34. Kleckner,N., Zickler,D., Jones,G.H., Dekker,J., Padmore,R., Henle,J. and Hutchinson,J. (2004) A mechanical basis for chromosome function. *Proc. Natl. Acad. Sci. U.S.A.*, **101**, 12592–12597.
35. Janke,C., Magiera,M.M., Rathfelder,N., Taxis,C., Reber,S., Maekawa,H., Moreno-Borchart,A., Doenges,G., Schwob,E., Schiebel,E. *et al.* (2004) A versatile toolbox for PCR-based tagging of yeast genes: new fluorescent proteins, more markers and promoter substitution cassettes. *Yeast*, **21**, 947–962.
36. Taxis,C. and Knop,M. (2006) System of centromeric, episomal and integrative vectors based on drug resistance markers for saccharomyces cerevisiae. *BioTechniques*, **40**, 73–78.
37. Wang,Y., Zhai,B., Tan,T., Yang,X., Zhang,J., Song,M., Tan,Y., Yang,X., Chu,T., Zhang,S. *et al.* (2021) ESA1 regulates meiotic chromosome axis and crossover frequency via acetylating histone h4. *Nucleic Acids Res.*, **49**, 9353–9373.
38. White,M.A., Wang,S., Zhang,L. and Kleckner,N. (2017) Quantitative modeling and automated analysis of meiotic recombination. *Methods Mol. Biol.*, **1471**, 305–323.
39. Achar,Y.J., Adhil,M., Choudhary,R., Gilbert,N. and Foiani,M. (2020) Negative supercoil at gene boundaries modulates gene topology. *Nature*, **577**, 701–705.
40. Langmead,B., Trapnell,C., Pop,M. and Salzberg,S.L. (2009) Ultrafast and memory-efficient alignment of short DNA sequences to the human genome. *Genome Biol.*, **10**, R25.
41. Ramírez,F., Ryan,D.P., Grüning,B., Bhardwaj,V., Kilpert,F., Richter,A.S., Heyne,S., Dündar,F. and Manke,T. (2016) deepTools2: a next generation web server for deep-sequencing data analysis. *Nucleic Acids Res.*, **44**, W160–W165.
42. Zhang,Y., Liu,T., Meyer,C.A., Eeckhoute,J., Johnson,D.S., Bernstein,B.E., Nusbaum,C., Myers,R.M., Brown,M., Li,W. *et al.* (2008) Model-based analysis of chip-Seq (MACS). *Genome Biol.*, **9**, R137.
43. Naughton,C., Avlonitis,N., Corless,S., Prendergast,J.G., Mati,I.K., Eijk,P.P., Cockroft,S.L., Bradley,M., Ylstra,B. and Gilbert,N. (2013) Transcription forms and remodels supercoiling domains unfolding large-scale chromatin structures. *Nat. Struct. Mol. Biol.*, **20**, 387–395.
44. Berłowska,J., Kregiel,D., Klimek,L., Orzeszyna,B and Ambroziak,W. (2006) Novel yeast cell dehydrogenase activity assay in situ. *Pol. J. Microbiol.*, **55**, 127–131.
45. Serrentino,M.E., Chaplais,E., Sommermeyer,V. and Borde,V. (2013) Differential association of the conserved SUMO ligase zip3 with meiotic double-strand break sites reveals regional variations in the outcome of meiotic recombination. *PLos Genet.*, **9**, e1003416.
46. Sturtevant,A.H.(1915) The behavior of the chromosomes as studied through linkage, *Z. Indukt. Abstamm. Vererbungsl.***13**, 234–287.
47. Muller,H.J. (1916) The mechanism of crossing-over. *Am. Nat.*, **50**, 193–221.
48. Wang,S., Hassold,T., Hunt,P., White,M.A., Zickler,D., Kleckner,N. and Zhang,L. (2017) Inefficient crossover maturation underlies elevated aneuploidy in human female meiosis. *Cell*, **168**, 977–989.
49. Liu,Y.X., Hsiung,Y., Jannatipour,M., Yeh,Y. and Nitiss,J.L. (1994) Yeast topoisomerase II mutants resistant to anti-topoisomerase agents: identification and characterization of new yeast topoisomerase II mutants selected for resistance to etoposide. *Cancer Res.*, **54**, 2943–2951.
50. Liu,Q. and Wang,J.C. (1999) Similarity in the catalysis of DNA breakage and rejoining by type IA and IIA DNA topoisomerases. *Proc. Natl. Acad. Sci. U.S.A.*, **96**, 881–886.
51. Liu,Q. and Wang,J.C. (1998) Identification of active site residues in the 'GyrA' half of yeast DNA topoisomerase iI. *J. Biol. Chem.*, **273**, 20252–20260.
52. Wasserman,R.A. and Wang,J.C. (1994) Mechanistic studies of amsacrine-resistant derivatives of DNA topoisomerase II.

Implications in resistance to multiple antitumor drugs targeting the enzyme. *J. Biol.Chem.*, **269**, 20943–20951.
53. Lindsley,J.E. and Wang,J.C. (1991) Proteolysis patterns of epitopically labeled yeast DNA topoisomerase II suggest an allosteric transition in the enzyme induced by ATP binding. *Proc. Natl. Acad. Sci. U.S.A.*, **88**, 10485–10489.
54. Baird,C.L., Harkins,T.T., Morris,S.K. and Lindsley,J.E. (1999) Topoisomerase II drives DNA transport by hydrolyzing one ATP. *Proc. Natl. Acad. Sci. U.S.A.*, **96**, 13685–13690.
55. Russell,L.B., Hunsicker,P.R., Kerley,M., Pyle,A. and Saxton,A.M. (2004) Etoposide exposure during male mouse pachytene has complex effects on crossing-over and causes nondisjunction. *Mutat. Res.*, **565**, 61–77.
56. Murakami,H., Lam,I., Huang,P.C., Song,J., van Overbeek,M and Keeney.,S. (2020) Multilayered mechanisms ensure that short chromosomes recombine in meiosis. *Nature*.,**582**, 124–128
57. Novak,J.E., Ross-Macdonald,P.B. and Roeder,G.S. (2001) The budding yeast msh4 protein functions in chromosome synapsis and the regulation of crossover distribution. *Genetics*, **158**, 1013–1025.
58. Heldrich,J., Sun,X., Vale-Silva,L.A., Markowitz,T.E. and Hochwagen,A. (2020) Topoisomerases modulate the timing of meiotic DNA breakage and chromosome morphogenesis in *saccharomycescerevisiae*. *Genetics*, **215**, 59–73.
59. Champoux.,J.J. (2001) DNA topoisomerases: structure, function and mechanism. *Annu. Rev. Biochem.*, **70**, 369–413.
60. Tse-DinhY.,C. (1998) Bacterial and archeal type i topoisomerases. *Biochim. Biophys. Acta.*, **1400**, 19–27.
61. Wang.,J.C. (1985) DNA topoisomerases. *Annu. Rev. Biochem.*, **54**, 665–697.
62. Perez-Cheeks,B.A., Lee,C., Hayama,R. and Marians,K.J. (2012) A role for topoisomerase III in escherichia coli chromosome segregation. *Mol. Microbiol.*, **86**, 1007–1022.
63. Deibler,R.W., Rahmati,S. and Zechiedrich,E.L. (2001) Topoisomerase IV, alone, unknots DNA in e. coli. *Genes Dev.*, **15**, 748–761.
64. Bermúdez,I., García-Martínez,J., Pérez-Ortín,J.E. and Roca,J. (2010) A method for genome-wide analysis of DNA helical tension by means of psoralen-DNA photobinding. *Nucleic Acids Res.*, **38**, e182.
65. Panizza,S., Mendoza,M.A., Berlinger,M., Huang,L., Nicolas,A., Shirahige,K. and Klein,F. (2011). Spo11-accessory proteins link double-strand break sites to the chromosome axis in early meiotic recombination. *Cell*., **146**, 372–383.
66. Sommermeyer,V., Béneut,C., Chaplais,E., Serrentino,M.E. and Borde,V. (2013). Spp1, a member of the set1 complex, promotes meiotic DSB formation in promoters by tethering histone H3K4 methylation sites to chromosome axes. *Mol. Cell.*, **49**, 43–54.
67. King,J.S. and Mortimer,R.K. (1990) A polymerization model of chiasma interference and corresponding computer simulation. *Genetics*, **126**, 1127–1138.
68. Fujitani,Y., Mori,S. and Kobayashi,I. (2002) A reaction-diffusion model for interference in meiotic crossing over. *Genetics*, **161**, 365–372.
69. Foss,E., Lande,R., Stahl,F.W. and Steinberg,C.M. (1993) Chiasma interference as a function of genetic distance. *Genetics*, **133**, 681–691.
70. Corless,S. and Gilbert,N. (2016) Effects of DNA supercoiling on chromatin architecture. *Biophys. Rev.*, **8**, 51–64.
71. Liang,Z., Zickler,D., Prentiss,M., Chang,F.S., Witz,G., Maeshima,K. and Kleckner,N. (2015) Chromosomes progress to metaphase in multiple discrete steps via global compaction/expansion cycles. *Cell*., **161**, 1124–1137.
72. Neguembor,M.V., Martin,L., Castells-García,Á., Gómez-García,P.A., Vicario,C., Carnevali,D., AlHaj Abed,J., Granados,A., Sebastian-Perez,R., Sottile,F. *et al.* (2021) Transcription-mediated supercoiling regulates genome folding and loop formation. *Mol. Cell*, **81**, 3065–3081.
73. Yu,H. and Dröge,P. (2014) Replication-induced supercoiling: a neglected DNA transaction regulator?*Trends Biochem. Sci.*, **39**, 219–220.
74. Cebrián,J., Castán,A., Martínez,V., Kadomatsu-Hermosa,M.J., Parra,C., Fernández-Nestosa,M.J., Schaerer,C., Hernández,P., Krimer,D.B. and Schvartzman,J.B. (2015) Direct evidence for the formation of precatenanes during DNA replication. *J. Biol. Chem.*, **290**, 13725–13735.
75. Wong,B.C., Chiu,S.K. and Chow,S.A. (1998) The role of negative superhelicity and length of homology in the formation of paranemic joints promoted by RecA protein. *J. Biol. Chem.*, **273**, 12120–12127.
76. Sun,W., Mao,C., Iwasaki,H., Kemper,B. and Seeman,N.C. (1999) No braiding of holliday junctions in positively supercoiled DNA molecules. *J. Mol. Biol.*, **294**, 683–699.
77. Lu,C.H. and Li,H.W. (2017) DNA with different local torsional states affects reca-mediated recombination progression. *ChemPhysChem*., **18**, 584–590.
78. Iwabata,K. and Sakaguchi,K. (2008) Lim15/Dmc1 enhances DNA topoisomerase II catenation activity independent of sequence homology. *Chromosoma*, **117**, 297–302.
79. Iwabata,K., Koshiyama,A., Yamaguchi,T., Sugawara,H., Hamada,F.N., Namekawa,S.H., Ishii,S., Ishizaki,T., Chiku,H., Nara,T. *et al.* (2005) DNA topoisomerase II interacts with lim15/dmc1 in meiosis. *Nucleic Acids Res.*, **33**, 5809–5818.
80. Travers,A. and Muskhelishvili,G. (2007). A common topology for bacterial and eukaryotic transcription initiation?*EMBO Rep.*, **8**, 147–151.
81. Kouzine,F., Sanford,S., Elisha-Feil,Z. and Levens,D. (2008). The functional response of upstream DNA to dynamic supercoiling in vivo. *Nat. Struct. Mol. Biol.*, **15**, 146–154.
82. Corless,S and Gilbert,N. (2016). Effects of DNA supercoiling on chromatin architecture. *Biophys. Rev.*, **8**, 51–64.
83. Morgan,C., Fozard,J.A., Hartley,M., Henderson,I.R., Bomblies,K. and Howard,M. (2021). Diffusion-mediated HEI10 coarsening can explain meiotic crossover positioning in *arabidopsis*. *Nat. Commun.*, **12**, 4674.
84. Zuo,W., Chen,G., Gao,Z., Li,S., Chen,Y., Huang,C., Chen,J., Chen,Z., Lei,M. and Bian,Q. (2021). Stage-resolved Hi-C analyses reveal meiotic chromosome organizational features influencing homolog alignment. *Nat. Commun.*, **12**, 5827.
85. Hinch,A.G., Zhang,G., Becker,P.W., Moralli,D., Hinch,R., Davies,B., Bowden,R. and Donnelly,P. (2019). Factors influencing meiotic recombination revealed by whole-genome sequencing of single sperm. *Science*, **363**, eaau8861.
86. Chen,Y., Lyu,R., Rong,B., Zheng,Y., Lin,Z., Dai,R., Zhang,X., Xie,N., Wang,S., Tang,F. *et al.* (2020). Refined spatial temporal epigenomic profiling reveals intrinsic connection between PRDM9-mediated H3K4me3 and the fate of double-stranded breaks. *Cell Res.*, **30**, 256–268.
87. Kouzine,F., Gupta,A., Baranello,L., Wojtowicz,D., Ben-Aissa,K., Liu,J., Przytycka,T.M. and Levens,D. (2013). Transcription-dependent dynamic supercoiling is a short-range genomic force. *Nat. Struct. Mol. Biol.*, **20**, 396–403.
88. Postow,L., Crisona,N.J., Peter,B.J., Hardy,C.D. and Cozzarelli,N.R. (2001) Topological challenges to DNA replication: conformations at the fork. *Proc. Natl. Acad. Sci. U.S.A.*, **98**, 8219–8226.
89. Chong,S., Chen,C., Ge,H. and Xie,X.S. (2014) Mechanism of transcriptional bursting in bacteria. *Cell*, **158**, 314–326.
90. Fernández,X., Díaz-Ingelmo,O., Martínez-García,B. and Roca,J. (2014) Chromatin regulates DNA torsional energy via topoisomerase II-mediated relaxation of positive supercoils. *EMBO J.*, **33**, 1492–1501.
91. Roca,J. (2011) Transcriptional inhibition by DNA torsional stress. *Transcription*, **2**, 82–85.
92. Jha,R.K., Levens,D. and Kouzine,F. (2022) Mechanical determinants of chromatin topology and gene expression. *Nucleus*, **13**, 94–115.
93. Garcia,V., Gray,S., Allison,R.M., Cooper,T.J. and Neale,M.J. (2015). Tel1(ATM)-mediated interference suppresses clustered meiotic double-strand-break formation. *Nature*, **520**, 114–118.
94. Zhang,L., Kim,K.P., Kleckner,N.E. and Storlazzi,A. (2011). Meiotic double-strand breaks occur once per pair of (sister) chromatids and, via Mec1/ATR and Tel1/ATM, once per quartet of chromatids. *Proc. Natl. Acad. Sci. U.S.A.*, **108**, 20036–20041.
95. Mohibullah,N. and Keeney,S. (2017). Numerical and spatial patterning of yeast meiotic DNA breaks by tel1. *Genome Res.*, **27**, 278–288.
96. Cooper,T.J., Garcia,V. and Neale,M.J. (2016). Meiotic DSB patterning: a multifaceted process. *Cell Cycle*, **15**, 13–21.